Direct electrochemical reduction of gas phase oxide and solid phase oxide; hydrodynamic / electrochemical approaches for effective reduction of nitrous oxide and silicon dioxide

기체 및 고체 상 산화물의 직접적인 전기화학적 환원법;

아산화질소 및 이산화규소의 효과적인 환원을 위한

유체역학적 / 전기화학적 접근

2022년 8월

서울대학교 대학원

화학생물공학부

김현수

Direct electrochemical reduction of gas phase oxide and solid phase oxide; hydrodynamic / electrochemical approaches for effective reduction of nitrous oxide and silicon dioxide

지도교수 김 재 정

이 논문을 공학박사 학위논문으로 제출함
2022년 8월

서울대학교 대학원
화학생물공학부
김 현 수

김현수의 박사 학위논문을 인준함
2022년   8월

위 원 장 _____ (인)

부위원장 _____ (인)

위   원 _____ (인)

위   원 _____ (인)

위   원 _____ (인)

Abstract

Nitrous oxide, a gaseous oxide studied in this research, is a powerful greenhouse gas with a global warming potential of 310 times that of carbon dioxide. Electrochemical reduction was used as reducing method of N_2O. Two approaches using electrochemical reduction were mainly applied for the effective electrochemical reduction of nitrous oxide. First, by applying a Couette-Taylor vortex reactor to an electrochemical system, it was attempted to increase the reaction rate of electrochemical reduction and the conversion rate of nitrous oxide through a hydrodynamic method. The solubility and dissolution rate of nitrous oxide showed a clear difference depending on the presence or absence of Taylor flow. Thereafter, the electrochemical reduction reaction of nitrous oxide was carried out in a Couette-Taylor vortex reactor to confirm the effect of the increased dissolution behavior on the electrochemical decomposition reaction. The conversion of nitrous oxide increased by 2.7 times compared to the absence of Taylor flow. Another approach to improve the electrochemical reduction of nitrous oxide was to apply an ionic liquid to the electrolyte. The ionic liquid used in this study was 1-butyl-3-methylimidazolium tetrafluoroborate, [BMIM][BF$_4$] as an electrolyte. The ionic liquid was used to exclude the hydrogen evolution reaction, which is a major side reaction in

the aqueous solution, and was mainly used as an electrolyte to increase the efficiency of the electrochemical reduction reaction. The low electrical conductivity and high viscosity of the ionic liquid act as disadvantages as an electrolyte, which could be minimized with the propylene carbonate. The current efficiency and the Faraday efficiency in the optimized ionic liquid electrolyte were 95% and 90%, respectively.

Another oxide studied in this research is SiO_2, a solid oxide. The electrochemical reduction reaction of silicon dioxide is possible by using 850°C $CaCl_2$ molten salt as an electrolyte. In addition, it was possible to improve the electrical contact through the formation of an Al-Si liquid alloy using Al metal and to make the reduced silicon form into a film form. Afterwards, optimization was performed by applying pulse reduction, which is used in the metal plating field. When reducing SiO_2 at the optimized time, a long reduction time, increased charge amount, and a thicker film were obtained. SEM and EDS analysis of the sample confirmed a flat film surface and more than 96% silicon component.

Keywords: electrochemical reduction, oxide, N_2O, Couette-Taylor vortex reactor, Taylor vortex, ionic liquid, [BMIM][BF₄], SiO_2, molten salt, Al-Si alloy, Si film

Student number: 2016-21022

Content

List of Tables

List of Figures

CHAPTER I

Introduction

1.1. Electrochemical reduction of oxide

The electrochemical reduction means that oxidant gets electrons from surface of a working electrode and reduced to reductant. There are lots of ways to reduce oxidant such as thermal or chemical methods, but the electrochemical reduction has some strong points compared to other methods. First, the electrochemical reduction reaction generally occurs near room temperature. Not to mention the thermal reaction, the chemical methods also need high temperature in order to increase the reaction rate [1, 2] Also, the efficiency of electrochemical reaction has potential for improvement through various process parameters such as electrode, catalyst, electrolyte, and applying electrical condition. Still, a lot of catalytic research for catalytic electrochemical reactions has been studied steadly[3, 4].

Generally, the electrochemical reduction reaction occurs like Fig. 1.1. The oxidant gets electrons near the surface of electrode, and turns to reductant. The rate of electrochemical reaction can be expressed in following equation (v = reaction rate, i =

current density, n = the number of involved electrons, F = Faradaic constant, A = electrode area, C(t) = concentration of reactant).

$$v = \frac{i}{nFA} = kC(t) \quad (1)$$

Because the reaction rate is directly affected by concentration of reactant, the increase of concentration can be helpful for effective chemical reaction. There are also many factors which can affect the reaction rate or efficiency such as electrode, electrolyte, electrochemical conditions, mass transfer, and etc [5, 6].
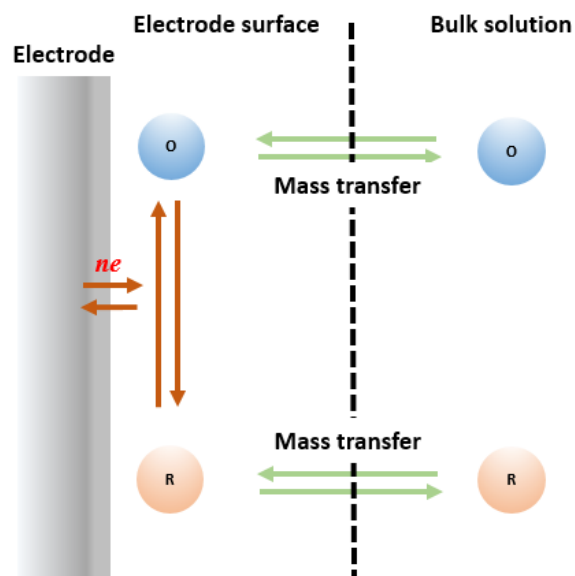
Figure 1.1. General electrochemical reaction mechanism near the electrode. Charge transfer between reactants and products.

1.2. Electrochemical reduction of N_2O with hydrodynamic approach

Nitrous oxide (N_2O) is a powerful greenhouse gas: it has a global warming potential that is 310 times that of CO_2 and is a dominant ozone-depleting substance[7, 8]. The global warming potential can be expressed in following equation.

$$GWP = \frac{heat\ absorbed\ by\ 1kg\ target\ gas}{heat\ absorbed\ by\ 1kg\ CO_2}$$

N_2O is emitted during various agricultural and industrial activities, such as cultivating crops in low-pH soil and manufacturing semiconductor devices (Fig. 1.2)[9, 10]. Especially, N_2O is widely used for making dielectric forming SiO_xN_y. The concentration of N_2O in the atmosphere has increased steadily, reaching a level that cannot be ignored anymore (Fig. 1.3)[10, 11]. Therefore, various methods for reducing N_2O emission are widely being studied.

Thermal decomposition of N_2O has been most widely reported to reduce N_2O emission. In this field, thermal catalysts have been considered as key to lowering the temperature of N_2O decomposition and increasing the conversion [12, 13]. Despite these efforts, however, the process temperature is still high (>250 °C). Maintaining a high process temperature is energetically inefficient.

Electrochemical reduction of N_2O is also an attractive way to reduce N_2O emission. Since it can take place at low temperatures, energy consumption for N_2O reduction can be minimized. Electrochemical reduction of N_2O in an aqueous solution occurs

according to the following reaction.

$$N_2O + H_2O + 2e^- \rightarrow N_2 + 2OH^- \quad (2)$$
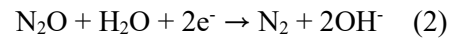
As mentioned in the previous section, the concentration of reactant is an important factor for efficient electrochemical reduction. In the case of N_2O reduction, the N_2O dissolution and solubility can be a critical parameter for effective reduction. Couette-Taylor vortex reactor (CTVR, Fig. 1.4) can be considered as an experimental apparatus for increasing the N_2O concentration in the aqueous solution[14]. In the reactor, the azimuthal viscous force and outward centrifugal force are applied to fluid inside of the reactor, and the solubility and dissolution of gases can be enhanced by Taylor vortex generated by the forces[15]. By adjusting the CTVR to electrochemical reduction system, it is possible to reduce N_2O electrochemically with Taylor vortex.
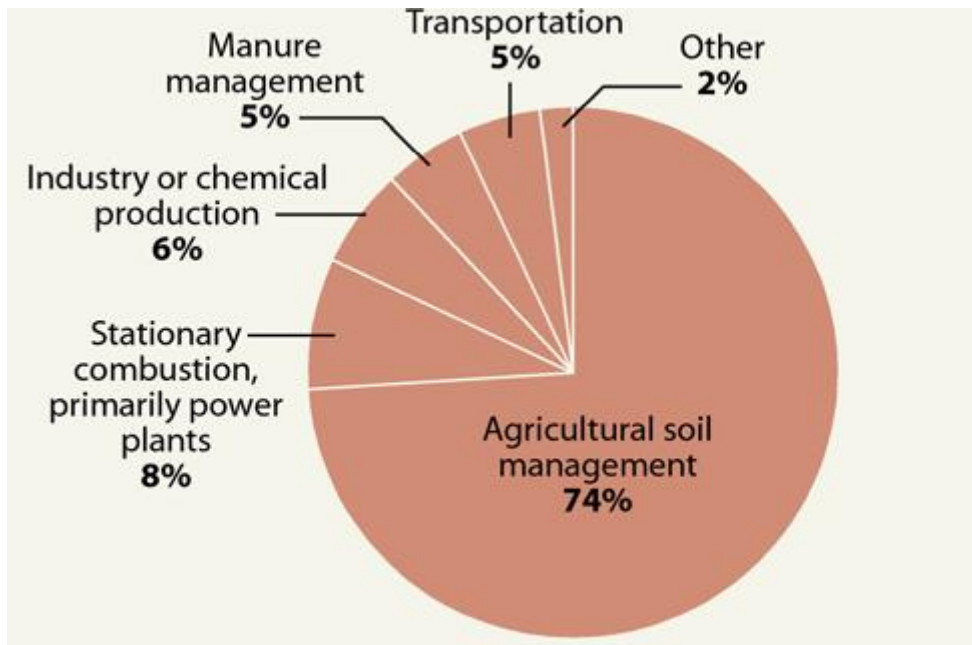
Figure 1.2. Where N_2O comes from (Ref. 10).
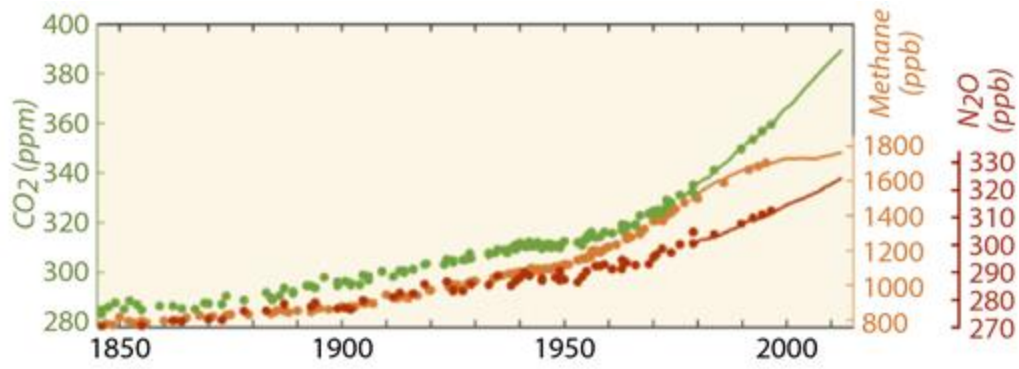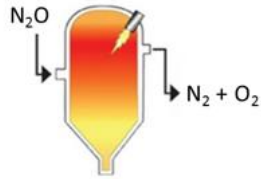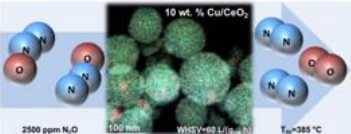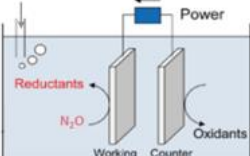
Figure 1.3. The trend of global greenhouse gases emission (Ref. 10).

Table 1.1. Various Methods for N2O Decomposition (Ref. 12, 13)

Thermal decomposition	Selective catalytic decomposition	Electrochemical decomposition
(> 1000°C)	(> 250°C)	(~25°C)

Figure 1.4. Couette-Taylor vortex reactor and forces applied to fluid in the reactor (Ref.

14).

1.3. Electrochemical reduction of N_2O with ionic liquid

In an aqueous solution, the electrochemical reduction of N_2O almost always involves hydrogen evolution because N_2O reduction and hydrogen evolution occur at similar potentials. This plays a major role in lowering the faradaic efficiency of N_2O reduction. Therefore, various electrocatalysts, such as metal Pd and In and metal oxides, have been studied for promoting N_2O reduction while suppressing the hydrogen evolution reaction (HER) [16-19]. Especially, Pd and In was effective catalysts for N_2O reduction (Fig. 1.5). However, few studies have focused on electrolytes instead of the catalysts. The HER is an inevitable process in aqueous electrolytes since water itself is a source of protons.

Ionic liquids are the material in the spotlight as an electrolyte in various electrical device industry such as refrigerant, cellulose dissolution, and fuel cell[20]. They have low volatility, low vapor pressure, and thermal stability which are advantageous properties in electrochemical reactions. The general structures of ionic liquids are shown in Fig. 1.6. Especially, the ionic liquids have no or little hydrogen ion when used as electrolyte, HER can be avoided during electrochemical reaction. Because the major side reaction of N_2O reduction is HER, ionic liquids can be a solution for effective electrochemical reduction of N_2O.
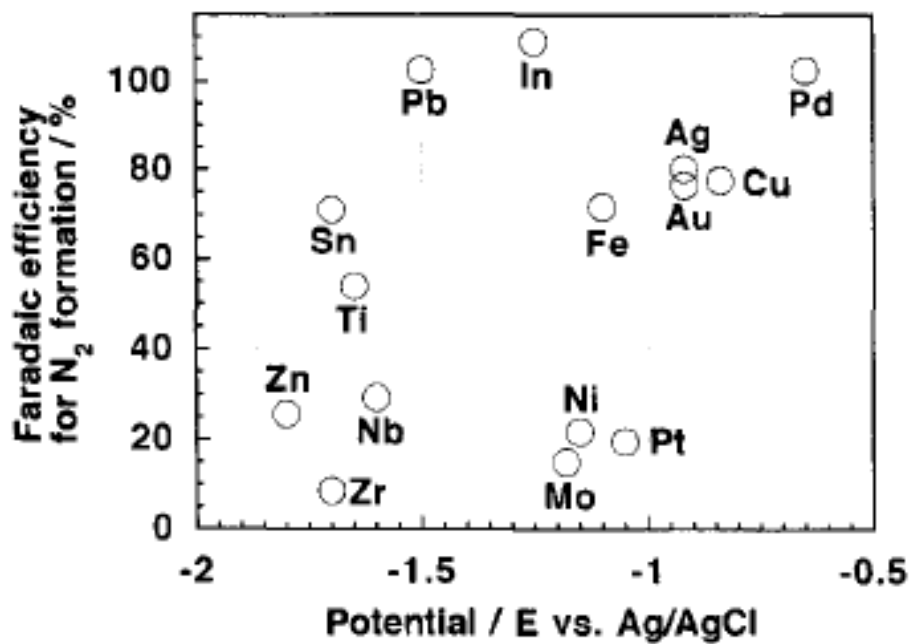
Figure 1.5. Various catalytic metals for electrochemical reduction of N_2O (Ref. 18).
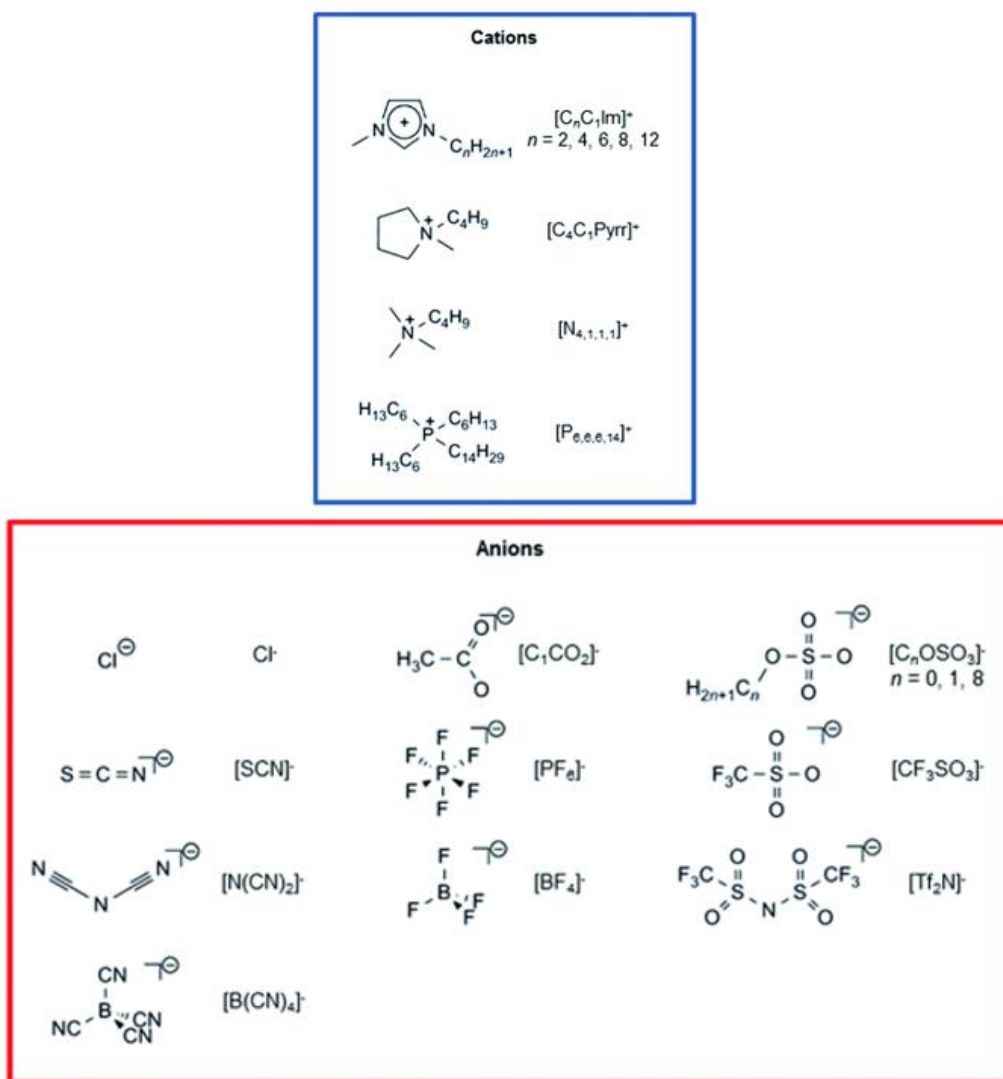
Figure 1.6. General structures of ionic liquids (Ref. 20)

1.4. Direct electrochemical reduction of SiO_2 in $CaCl_2$ molten salt

Si, which has useful properties such as good chemical stability and electrical tunability, is an essential semiconductor material for electronic and photovoltaic devices such as transistors, integrated circuits, solar cells and sensors [21, 22]. Si is abundant on Earth, but most Si exists in the form of SiO_2, one of the most chemically stable substances. Therefore, it requires a lot of energy and cost to extract Si from SiO_2 [23]. Afterwards, in order to obtain high-purity Si, a complicated and energy-intensive process is additionally required in the Si purification step [24-26]. To address this issue, many investigations have been conducted to produce Si through a more cost-effective and simple process. Cost-effective Si production would contribute to the development of Si-based electronic and photovoltaic device industry. One promising approach is the direct electrochemical reduction of SiO_2, as shown in equation 3. Through the study of the direct electrochemical reduction pathway, as shown in Fig. 1.7, it is possible to achieve simplification and energy saving of many complex process[27].

$$SiO_2 + 4e^- \rightarrow Si + 2O^{2-} \qquad (3)$$
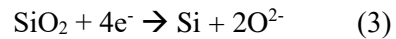
There are many studies on the electrochemical reduction of SiO_2 using various electrolytes such as molten salts, organic solvents, and ionic liquids [28-31]. Nohira, et. al.

reported direct electrochemical reduction of bulk SiO_2 in a $CaCl_2$ molten salt, which is capable of dissolving a significant amount of oxygen ions (O^{2-} ions) generated during the reduction process (Fig. 1.8)[32]. After that, many trials to reduce SiO_2 were reported in various molten salts ($CaCl_2$, LiF-KF, and KCl-KF) and on various substrates (Mo, Ag, and C) [33-36]. Electrochemical reduction of SiO_2 is a difficult process because SiO_2 is a non-conductive material and has a high reduction potential [37, 38]. It is also necessary to provide a path for O^{2-} ions to escape from the SiO_2 matrix during the reduction process because the accumulation of O^{2-} ions at the reducing surface can lead to the formation of unwanted oxides [39, 40]. Therefore, in order to facilitate the SiO_2 reduction, it is very important to uniformly and widely form a three-phase interface where SiO_2, a conductor capable of providing electrons, and an electrolyte can meet together. Another challenge is the separation of the Si product. Since most of Si formed from SiO_2 has a porous and/or particulate structure and bonds with unreacted SiO_2, it is difficult to completely separate the product Si from the residual SiO_2 and molten salt. These problems can be solved to some extent by using SiO_2 nanoparticles (~15 nm in diameter) dispersed in electrolyte as a source for electrochemical reduction [41, 42]. This method can not only extend the three-phase interface, but also selectively precipitate Si on the electrode. However, the price of SiO_2 nanoparticles is quite high compared to normal SiO_2 particles

(1-10 μm in diameter) and it is difficult to maintain uniform dispersion of SiO_2 nanoparticles in high-temperature molten salt.

Since most Si-based devices require high-purity Si, the purity of Si obtained by the electrochemical reduction is also an important issue. It was reported that high-purity Si was obtained when SiO_2 was electrochemically reduced on Ag. In the course of the reduction, Ag reacts with Si to form liquid-state Ag-Si alloys droplets which act as nucleation sites for Si growth in 850 °C molten $CaCl_2$ [43]. Si formed by SiO_2 reduction is regenerated through supersaturation and precipitation through Ag-Si droplets, leading to one-dimensional growth of Si, which is similar to VLS (vapor-liquid-solid method) mechanism (Fig. 1.9)[44]. Si formed in this way has high purity, but has an irregular morphology and is difficult to control. On the other hand, SiO_2 particles were reduced to Si film on graphite substrate (Fig. 1.10)[45]. Through these studies, it could be expected that morphology of reduced Si is able to be controlled by using other substrate or metal species.
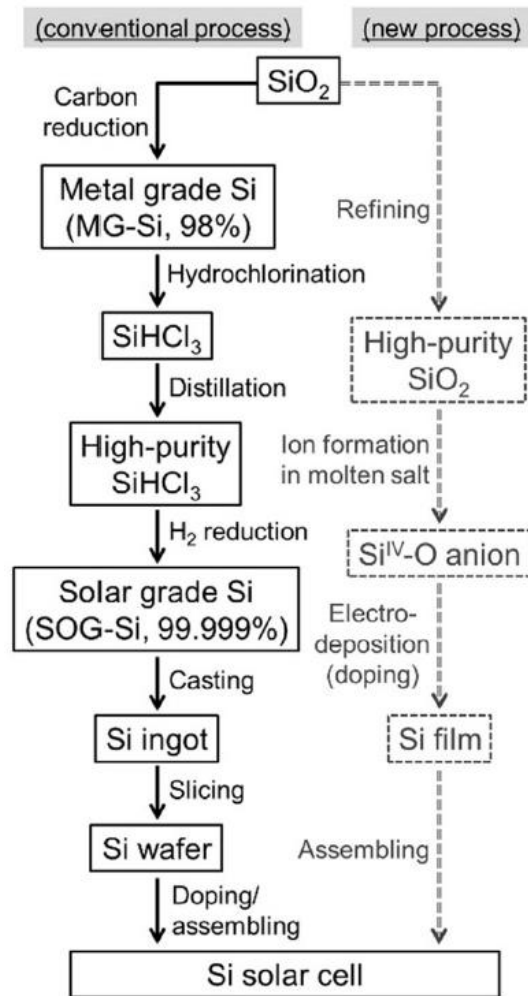
Figure 1.7. Conventional pure Si production process and electrochemical reduction process (Ref. 29).
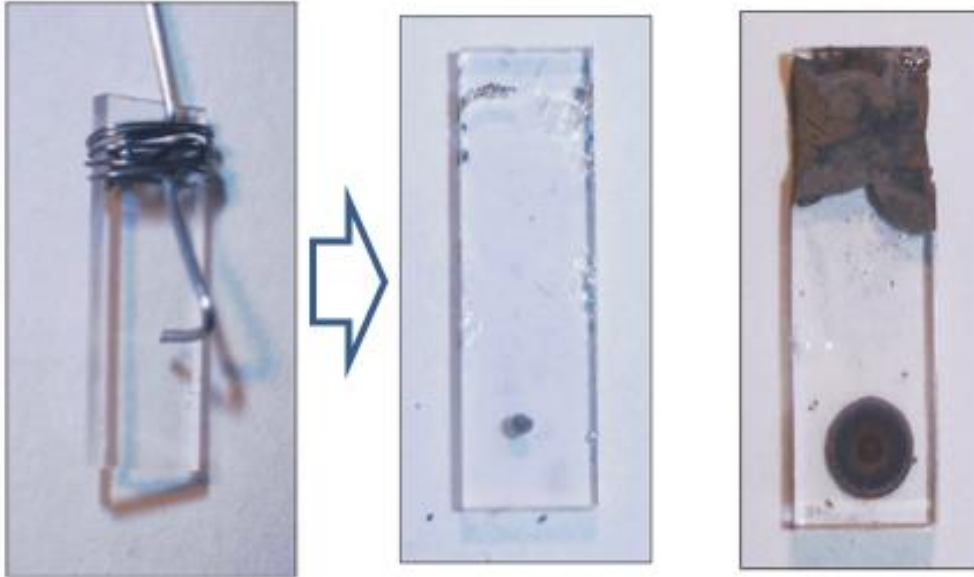
Figure 1.8. Direct electrochemical reduction of SiO_2 with molybdenum wire working

electrode (Ref. 27).
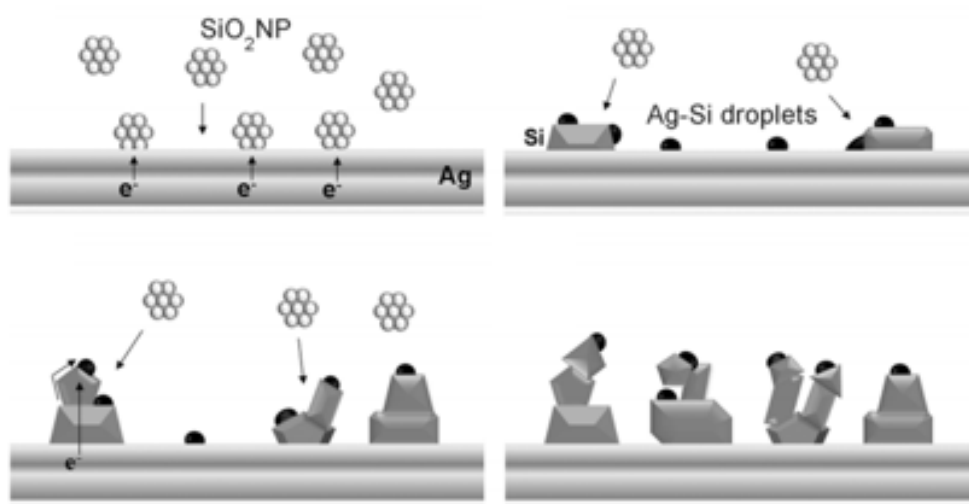
Figure 1.9. Mechanism of Si wire formation during electrochemical reduction of SiO_2

with Ag-Si eutectic formation (Ref. 44).
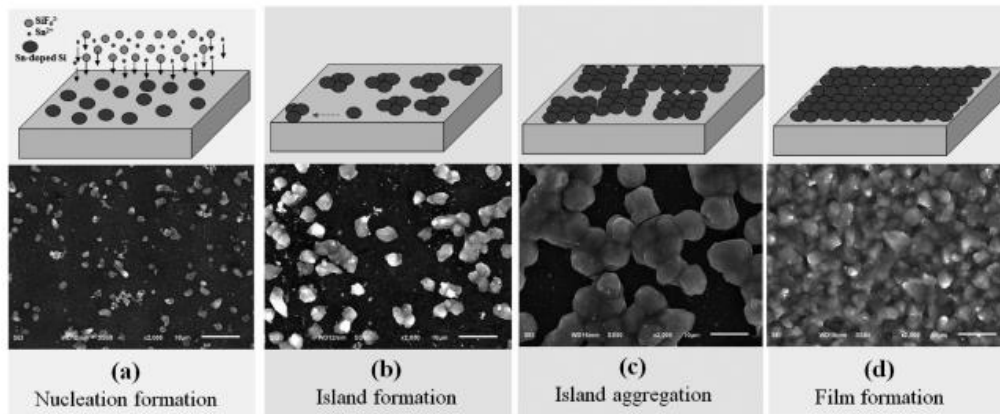
Figure 1.10. Mechanism of Si film formation during electrochemical reduction of SiO_2

on graphite substrate (Ref. 45).

1.5. Purpose of this study

In this study, various hydrodynamic and electrochemical approaches were studied for effective reduction of gas and solid phase oxides, N_2O and SiO_2 each. For electrochemical reduction of N_2O, a Couette-Taylor vortex reactor was set as electrochemical reduction system. The solubility and dissolution of N_2O rate was anticipated to increase caused by Taylor vortex. Measurement of N_2O concentration in the electrolyte could show the effect or Taylor vortex on N_2O dissolution in aqueous solution. The increased N_2O concentration and dissolution rate were directly connected to the electrochemical reaction performance. By measuring the conversion of N_2O through gas chromatograpy, the enhancing effect of Taylor vortex on electrochemical reduction was investigated.

As well as the hydrodynamic approach, effective electrochemical reduction of N_2O was conducted using an ionic liquid/organic solvent solution as the electrolyte. 1-Butyl-3-methylimidazolium tetrafluoroborate ([BMIM][BF$_4$]) has been reported as an effective ionic liquid for dissolving N_2O up to a concentration of 2.18 $mol \cdot kg_{IL}^{-1}$, which is 90 times the solubility offered by water (Table. 1.2)[46, 47]. The high viscosity and low electrical conductivity of the ionic liquid, which significantly hinder the electrolysis,

were controlled by adding propylene carbonate (PC). Through composition optimization of the [BMIM][BF$_4$]/PC solution, effective N$_2$O reduction could be achieved in terms of current density and faradaic efficiency. To the best of our knowledge, this is the first attempt to use an ionic liquid for the electrochemical reduction of N$_2$O.

About solid phase oxide, the electrochemical reduction of SiO$_2$ particles in 850 $^\circ$C molten CaCl$_2$ was performed using Al instead of Ag as a material capable of forming liquid alloys with Si. Al is a promising metal for forming alloys with Si because of its low alloying point, low cost, and low surface tension at process temperature compared with Ag [48, 49]. Al is also expected to enhance the electrical contact between surface of working electrode and SiO$_2$ because it exists in a liquid state in the CaCl$_2$ molten salt due to its low melting point. The phase diagram of Al-Si system was shown in Fig. 1.11[50]. We also employed a pulse electrochemical reduction technique for the SiO$_2$ reduction to allocate sufficient time for O^{2-} ions to diffuse away from the reducing surface during off time [51]. By optimizing the on/off time of pulse electrochemical reduction, a continuous and dense Si film was obtained from SiO$_2$ particles.

Table 1.2. Solubility of N_2O in various ionic liquids (Ref. 46)

ILs	x_{N_2O}	molality ($mol_{N_2O} \cdot kg_{IL}^{-1}$)
[BMIM][BF$_4$]	0.33	2.18
[BMIM][SCN]	0.15	0.90
[DMIM][MP]	0.18	1.14
[(OH)$_2$IM][Tf$_2$N]	0.40	1.75
[(ETO)$_2$IM][Tf$_2$N]	0.51	2.38
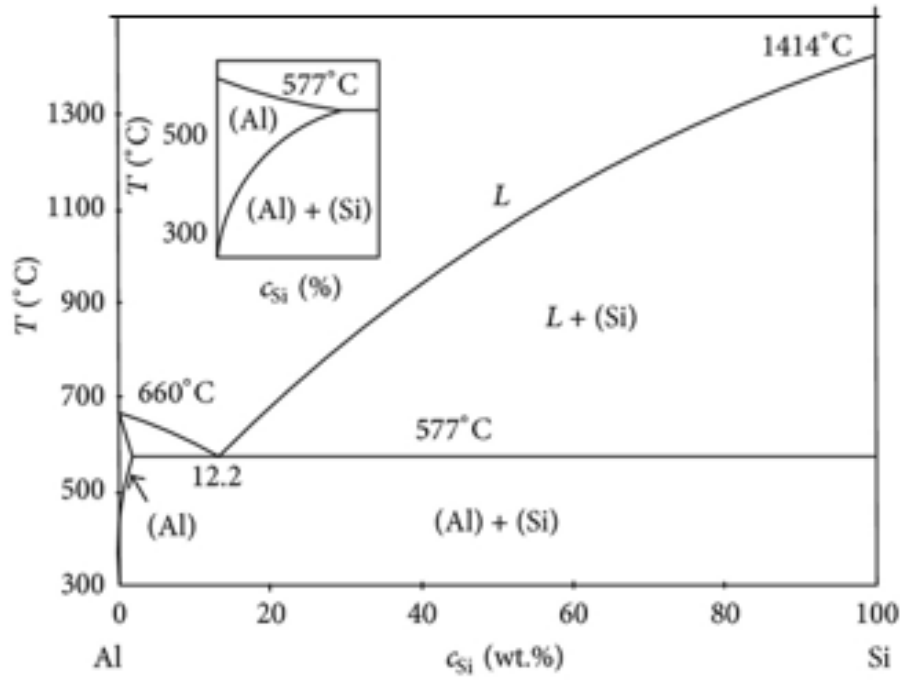
Figure 1.11. Phase diagram of Al-Si system (Ref. 50).

CHAPTER II

Experimental

2.1. Measurement of N$_2$O dissolution

The CTVR was used for increasing the N$_2$O dissolution and as electrochemical system itself. The apparatus was shown in Fig. 2.1. When we evaluate the dissolution rate and solubility of N$_2$O, the glass cylinder, which was transparent for observing the vortex flow, was used. Electrochemical reduction was conducted with SUS cylinder. The concentration of N$_2$O in the solution was measured with cyclic voltammetry. The working electrode was a Pd disk electrode and counter electrode was Pt wire. Saturated calomel electrode (SCE; KCl saturated, CHI150, CHI instruments, USA) was used as reference electrode. Solubility of N$_2$O at 25°C was known as 24.3 mM[52]. After saturation, the solutions were diluted into various N$_2$O concentration (0, 4.86, 9.72, 14.6, 19.4, 24.3 mM) and cyclic voltammograms were acquired in a potential range of 1.0 to -1.0 (Fig. 2.2a). The scan rate was 50 mV s^{-1} using a potentiostat (model 263A, EG&G, Princeton Applied Research, USA). A calibration curve of N$_2$O concentration and peak current density was acquired (Fig. 2.2b). Using this calibration curve, concentration of N$_2$O could be calculated by simply getting an CV graph.

2.2. Electrochemical analysis

The electrochemical reduction system was set as shown in Fig. 2.3. The working

electrode was Cu foil (250 cm^2), and counter electrode was SUS inner cylinder (440 cm^2).

The Cu foil was attached inside of outer SUS cylinder and connected to power supply

(XG 33-25, Sorensen^{TM}). Two electrode system was adopted and electrolyte was 0.3 M

K_2SO_4, 0.01 M KOH (pH 12). 25°C was maintained with cooling system during whole

experiments. Rotational speed of inner cylinder was 0 and 1000 rpm for batch system

and Taylor vortex system each. Inlet gas flow rate was 6.4, 15, 75 ccm and applied

current was 1.0, 3.0, 5.0 A. Pd whisker catalyst was synthesized with galvanic

displacement reaction in $PdSO_2$ solution with Cu foil. The solution contained 3 mM

$PdSO_4$ (99.99%, Alfa Aesar) and 0.1 M $HClO_4$ (70%, Junsei). The displacement reaction

was carried out at 25 ^{o}C for 5 min.

The electrochemical reduction of N_2O in [BMIM][BF$_4$]/PC solution was evaluated by

linear sweep voltammetry (LSV) and cyclic voltammetry (CV) at a scan rate of 50 mV

s^{-1} using a potentiostat (model 263A, EG&G, Princeton Applied Research, USA). The

working electrode was a Cu electrode (0.196 cm^2). A Pt wire and saturated calomel

electrode (SCE; KCl saturated, CHI150, CHI instruments, USA) served as the counter

and reference electrodes, respectively. For comparison, electrochemical reduction of

N_2O in aqueous phase was performed in a 0.3 M K_2SO_4 (>99.0%, Daejung Chemicals

& Metals Co., LTD., Republic of Korea) aqueous solution. Prior to the experiment, N_2O

(99.999% purity, Deokyang Co., LTD., Republic of Korea) or Ar (99.9% purity,

Deokyang Co., LTD., Republic of Korea) purging was carried out in the solutions for at

least 1 h.

In the direct electrochemical reduction of SiO_2, Fig. 2.4 and 2.5 shows the schematic

diagram and optical image of the electrochemical cell used in this study. The vessel

consisted of a cylindrical alumina crucible (diameter (D): 42 mm, length (L): 60 mm), a

quartz tube (D: 46 mm, L: 200 mm) closed at one end, and a quartz-flanged tube (D: 52

mm, L: 500 mm) closed at one end, in order from the innermost. The vessel was tightly

sealed with a stainless steel lid. The working electrode (WE) was a graphite crucible (D:

8 mm, L: 15 mm), and graphite rods (D: 6mm, L: 38 mm) were used as the counter

electrode (CE) and quasireference electrode (QRE). The electrodes were inserted into

the vessel through the holes of the stainless steel lid. During the experiment, the inside

of the vessel was maintained in an Ar atmosphere through the continuous supply of Ar

gas (99.999%). All electrodes were connected to a potentiostat (model 263A, EG&G,

Princeton Applied Research, USA) via tungsten wires (D: 1 mm, L: 700 mm). The vessel temperature was maintained at 850°C using a vertical tube furnace (DTF-60900 APYS, Daeheung Science).

CaCl$_2$·2H$_2$O (99%, Daejung chemicals & metals co. LTD.) was dehydrated at 200°C in a vacuum oven for over 12 hours before use. 50 g of dehydrated CaCl$_2$ was placed in a cylindrical alumina crucible. After assembling the electrochemical cell with the CaCl$_2$-containing alumina crucible, further drying was performed at 400 °C for 2 hours under vacuum to remove residual moisture in CaCl$_2$. The electrochemical cell was then heated to 850°C in an Ar atmosphere. The graphite crucible containing 0.2 g of SiO$_2$ particles (1-5 μm, 99%, Aldrich) and Al foil (0.016-mm-thick, 99.999%, Lotte Aluminum co. LTD.) was immersed in the molten CaCl$_2$ at 850°C. Cyclic voltammetry (CV) was performed in a potential range of 0 – -1.4 V (vs. graphite QRE) at a scan rate of 50 mV s^{-1}. The electrochemical reduction of SiO$_2$ particles was conducted by applying a constant reduction current of 60 mA or a pulsed reduction current with current amplitude of 60 mA.

2.3. Optimization of experimental conditions and electrolyte

In Chapter 3.2, The composition of [BMIM][BF$_4$]/PC was controlled by modifying the ratio of [BMIM][BF$_4$] (>98.0% purity, Sigma-Aldrich, USA) and PC (>99.7% purity, Sigma-Aldrich, USA). The residual water in [BMIM][BF$_4$] was removed for at least 12 h in a vacuum oven at 80 °C before use. The structure of [BMIM][BF$_4$] is shown in Fig. 1b. The viscosity was measured with a viscometer (model LP-22, Brookfield, USA). The solution resistance was measured with electrochemical impedance spectroscopy (Versastat II, EG&G, Princeton Applied Research, USA) in the frequency range of 100 Hz to 1 MHz. The electrical conductivity was calculated from the solution resistance. The applied potential during chronoamperometry was −1.9 V (in [BMIM][BF$_4$]/PC solution) and −1.3 V (in aqueous solution). The potential was the point that showed the highest current density of N$_2$O reduction in each medium. A Cu foil (99.98% purity, 0.025 mm thick, 1.4 cm × 1.0 cm, Sigma-Aldrich, USA) was used as working electrode, and a Pt wire and SCE was counter and reference electrodes respectively.

In Chapter 3.3, The on off time were adjusted for the optimization of the SiO$_2$

reduction. On/off time ratios were 1000/125, 500/125, 250/125, 125/125, 63/125, 32/125

s. applied current was 60 mA during the chronopotentiometry with a potentiostat (model

263A, EG&G, Princeton Applied Research, USA).

2.4. Properties and performance

In chapter 3.1, the conversion values were compared with each electrochemical reduction conditions. The conversion of N_2O was calculated with following equation (Q_i: inlet flow rate, Q_o: outlet flow rate, X_i: inlet N_2O concentration, X_o: outlet N_2O concentration).

$$\text{Conversion} = \frac{Q_i X_i - Q_o X_o}{Q_i X_i} \qquad (4)$$

In Chapter 3.2, Current efficiency was calculated from the reduction current density recorded in the solution with or without N_2O gas purging (i_{N2O} and i_{BG}, respectively).

$$\text{Current efficiency} = \frac{(i_{N2O} - i_{BG})}{i_{N2O}} \qquad (5)$$

Faradaic efficiency was calculated based on the amount of product gas (N_2) measured by GC (GC 5890 SERIES II+, Hewlett Packard, USA). During the chronoamperomentry, 1 cm^3 of outlet gas was sampled and analyzed with a thermal conductivity detector after 3600 s of operation.

In Chapter 3.3, After electrochemical reduction, the working electrode (graphite crucible) was carefully removed from the electrochemical cell and immersed in deionized water to dissolve the solidified $CaCl_2$ to separate the product Si. Then, the

separated Si was sequentially immersed in 1 M HCl aqueous solution (35%, Daejung

chemicals & metals co. LTD.) for 12 hours and 0.5 vol% HF aqueous solution (48%, J.T.

Baker) for 5 min to remove residues such as Al and unreacted SiO_2. The Si products

were characterized by field emission scanning electron microscope (FE-SEM, MERLIN

Compact, ZEISS) equipped with energy dispersive spectroscopy system (EDS, INCA

Energy, Oxford Instruments Analytical LTD.) and X-ray diffraction (XRD, D8

Advance.2020, Bruker, US).
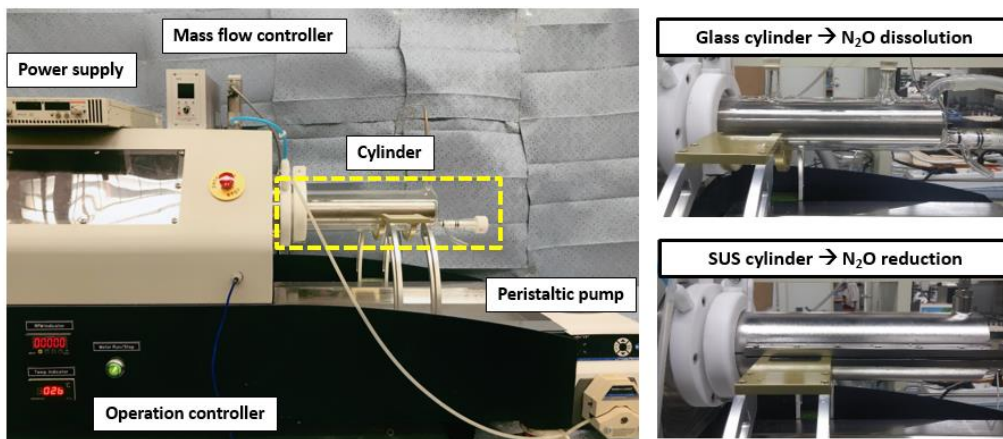
Figure 2.1. CTVR used for N₂O dissolution (glass cylinder) and electrochemical

system (SUS cylinder).
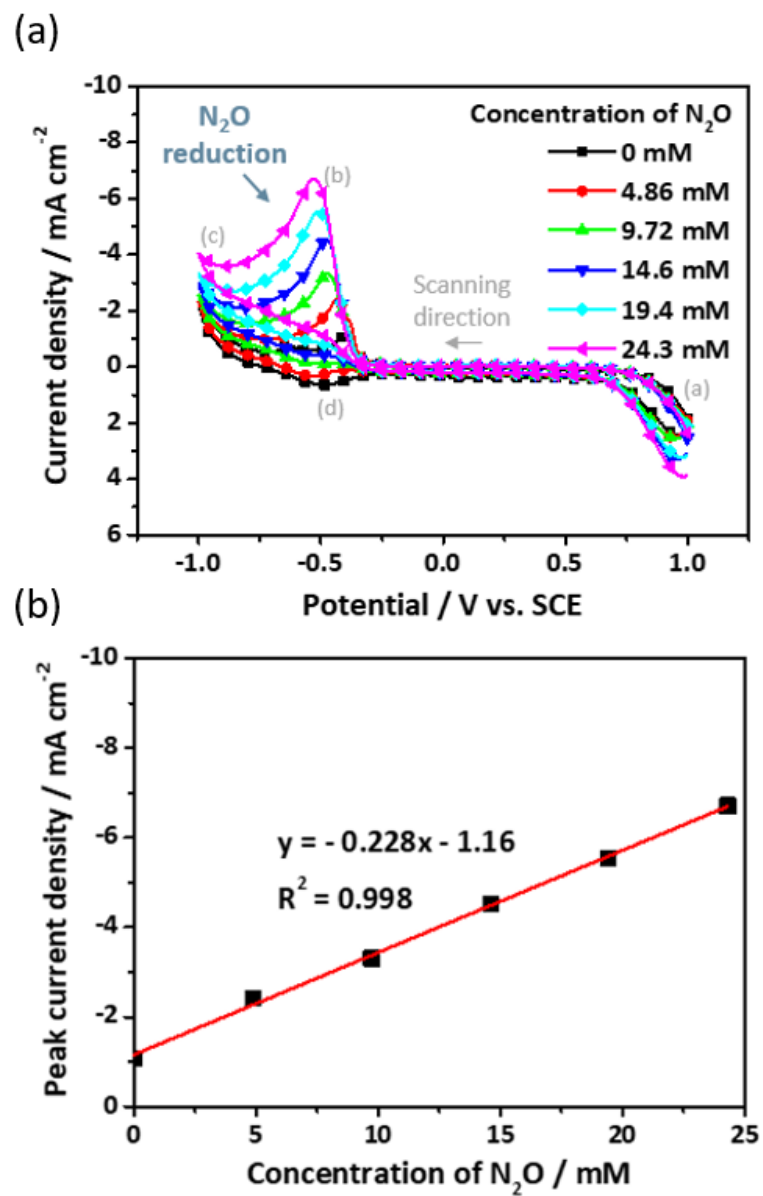
Figure 2.2. (a) Cyclic voltammograms of solutions containing various concentrations

of N₂O. (b) Calibration curved of concentration of N₂O and peak current density.
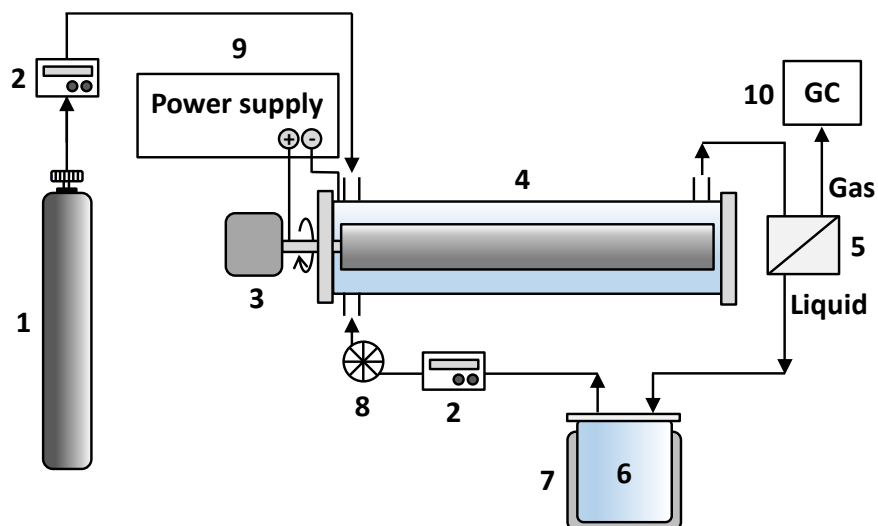
Figure 2.3. Scheme of electrochemical reduction system with CTVR. ((1) N_2O gas cylinder, (2) mass flow controller, (3) motor, (4) CTF mixer, (5) gas-liquid separator, (6) bath with outlet solution, (7) cooling jacket, (8) peristaltic pump, (9) power supply, (10) gas chromatography)
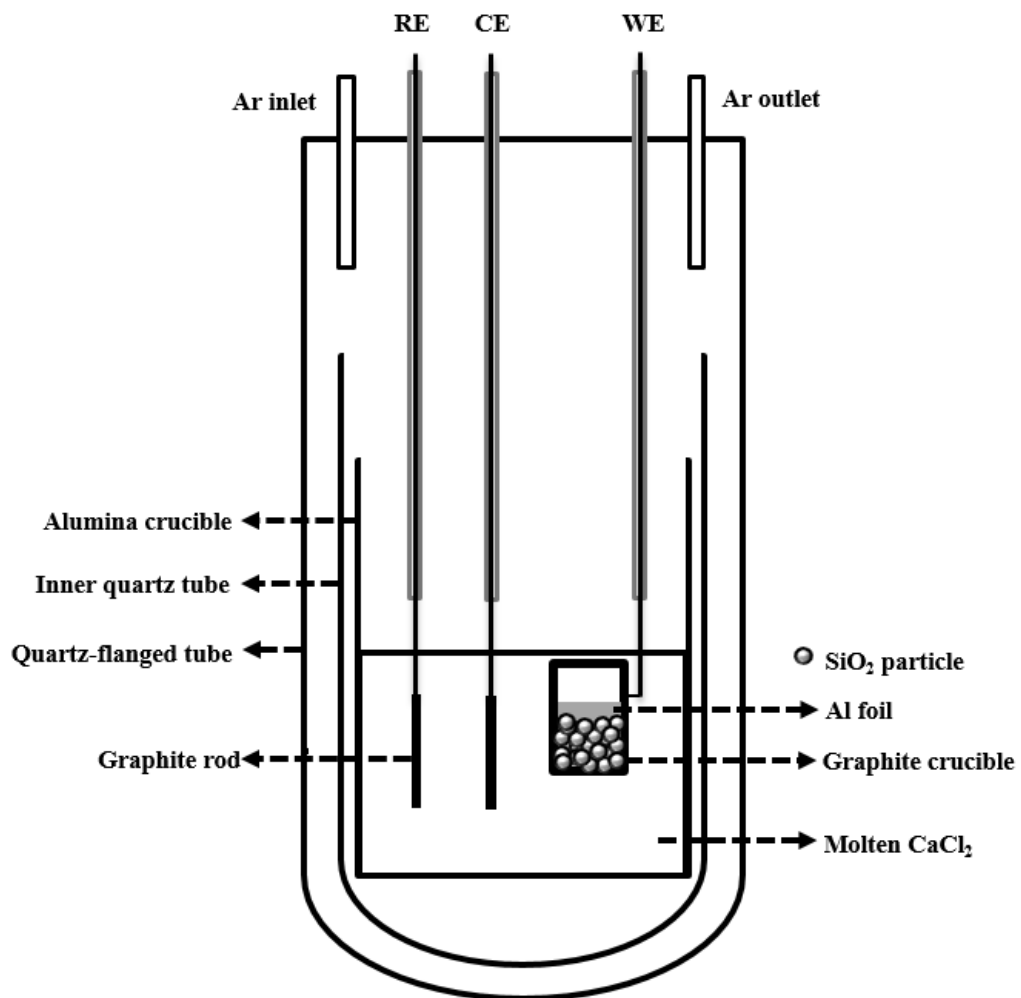
Figure 2.4. Schematic diagram of experimental apparatus for the molten salt electrodeposition.

Figure 2.5. Optical image of electrochemical system for SiO_2 reduction in $CaCl_2$ molten salt.

CHAPTER III

Results and Discussion

3.1 Electrochemical reduction of N_2O in CTVR

3.1.1. The effect of the CTVR on N_2O dissolution

The relationship of N_2O concentration and rotational speed of inner cylinder was studied[17] (Fig. 3.1). At the rotational speed of 1000 rpm where the Taylor number was 3229, the concentration of N_2O was the highest value. With this results, it could be presumed that the Taylor vortex occurred when the rotational speed was 1000 rpm. At the same reactor, N_2O dissolution was compared between the 0 rpm batch system condition and 1000 rpm CTVR system condition (Fig. 3.2). Table. 3.2, the saturation time was remarkably shortened from 30 min to 2 min with 1000 rpm, and saturated concentration of N_2O was 30.5 mM which was 27% higher than batch system (Table 3.1). The Taylor vortex seemed to bring two major advantages for N_2O dissolution. First is increasing volumetric diffusion coefficient by intensive mixing. The volumetric diffusion coefficient, k_La increases as the rotational speed increases (Fig. 3.3)[53]. When the charge transfer is limited, the mass transfer rate also affects the electrochemical

reaction rate. Therefore, the Taylor vortex could enhance the N_2O transport to the surface of Cu working electrode and increase the reaction rate. And the other advantage is the increase of N_2O solubility. At the same temperature, the solubility of gas is affected by gas pressure. According to the previous study, the Taylor vortex also made bubble size small (Fig. 3.4)[54]. With the relationship between the pressure and radius of the bubble as shown in following equation, the bubble pressure could be increased as bubble size decrease (p_i: inside partial pressure, p_o: outside partial pressure, γ: surface tension, r: radius of bubble).

$$\mathrm{p}_i - \mathrm{p}_o = \frac{4\gamma}{r} \qquad (6)$$

The increase of bubble pressure also brings the increase of N_2O solubility as a result. With the two major advantages, the N_2O dissolution could be enhanced and it was expected to contribute to the electrochemical reduction performance also.

3.1.2. Conversion of N_2O with CTVR system

In order to measure the conversion of N_2O, the concentration of N_2O in outlet gas should be also measured, and gas chromatograpy (GC) was used for the measurement. Standard N_2O gases were used for calibration curve and the peak area of N_2O was investigated with GC. Calibration curves were obtained from the GC analysis in high concentration range and low concentration range (Fig. 3.5).

Electrochemical reduction of N_2O was conducted with various condition. At first, the batch system and CTVR system was compared in the terms of conversion. The applied potential was 3.5 V and inlet gas flow rate was 15 ccm. The conversion change was shown in Fig. 3.6. The N_2O conversions were 4.2% and 11.2% at 0 rpm and 1000 rpm each. The increase in conversion rate greatly outweighs the increase in solubility. From this result, the remarkable increase of dissolution rate seemed to affect the conversion dominantly. Because the reduction system was continuous flow system, the rate that N_2O dissolves in solution seemed important factor.

After that, the effect of other parameters was also investigated. At 3 A and 1000 rpm condition, the inlet flow rate was changed as 6.4, 15, and 75 ccm (Fig. 3.7a). High flow rate means larger amount of N_2O should be reduced in the same system and condition.

As a result, the conversion of N_2O decreased as the flow rate increased. For the other reduction parameter, the applied current was also changed as 1.0, 3.0, and 5.0 A (Fig. 3.7b). Contrary to the common sense that the larger the current, the faster the reaction rate, the actual conversion rate was high at low current. As mentioned before, N_2O reduction occurs competitively with HER, and HER becomes more dominant at high electrical potential. Therefore, the high applied current increases only the reaction rate of HER, and the reaction site on the electrode surface where N_2O reduction occurs is reduced due to the generated hydrogen gas.

Afterwards, in order to further increase of the conversion rate, various process variables including the inlet N_2O concentration were adjusted, and a higher conversion rate was obtained by applying the Pd whisker catalyst produced in the previous study in this laboratory[16, 55]. The main results are summarized in Table 3.1. Using a Pd whisker, when the N_2O throughput was lowered by the concentration and flow rate and a static potential was applied, a high conversion rate of 96% was obtained.
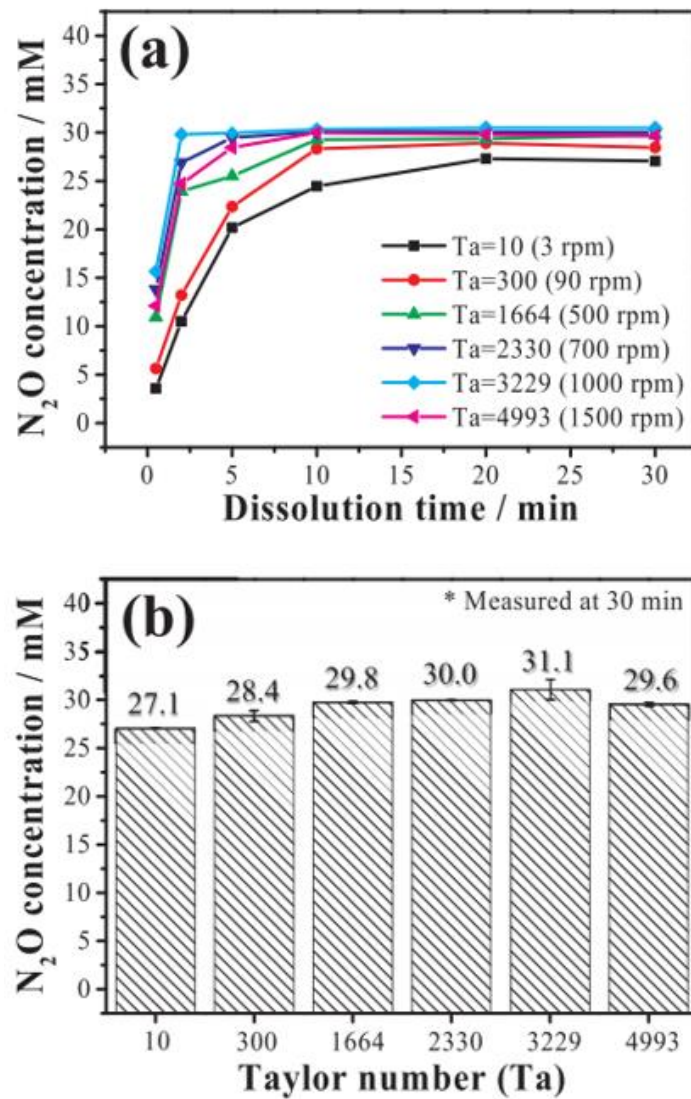
Figure 3.1. (a) N_2O concentration measured over N_2O dissolution time at various Ta number, and (b) saturated N_2O concentration obtained at each Ta number (Ref. 17).
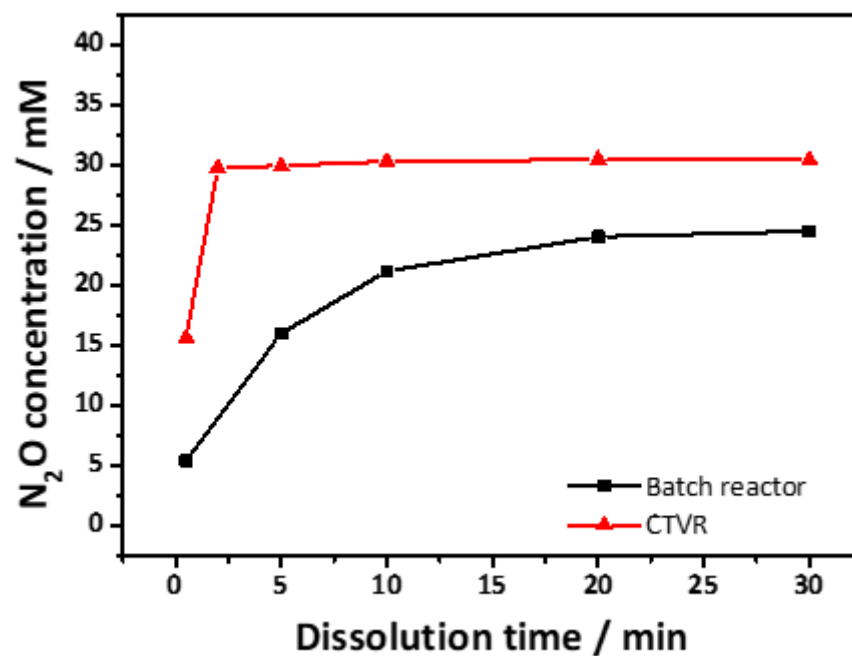
Figure 3.2. N$_2$O dissolution at 0 rpm batch system condition and 1000 rpm CTVR condition.

Table 3.1. The Saturation Time and Solubility of N_2O at 0 rpm Batch System Condition

and 1000 rpm CTVR Condition.

	Batch	CTVR
Saturation time	30 min	2 min
Solubility	24.3 mM	30.5 mM
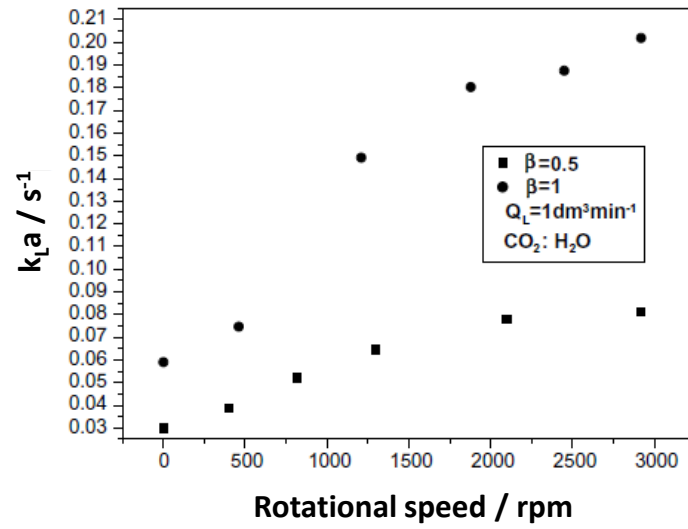
Figure 3.3. Volumetric diffusion coefficient (k_La) with rotational speed (Ref. 53). (β:

volumetric flow ratio of gas and liquid, Q_L: volumetric liquid flow rate)
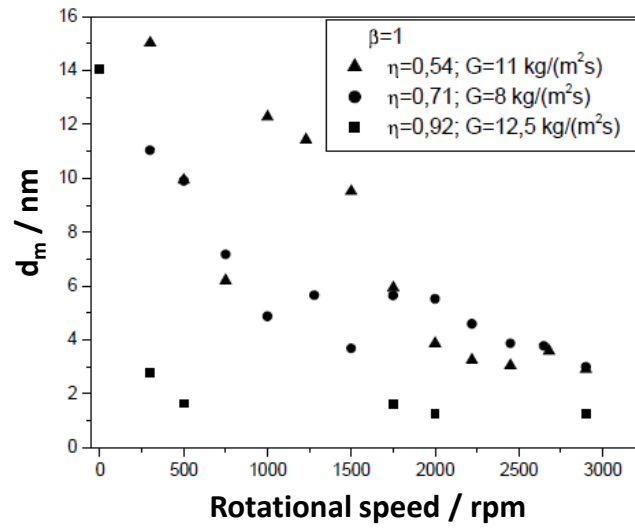
Figure 3.4. Bubble size (d_m) expressed in diameter with rotational speed change (Ref. 54). ($\eta = D_i/D_O$ ratio of the rotor (D_i) and outer cylinder (D_o) diameters, G: axial mass flux of liquid)
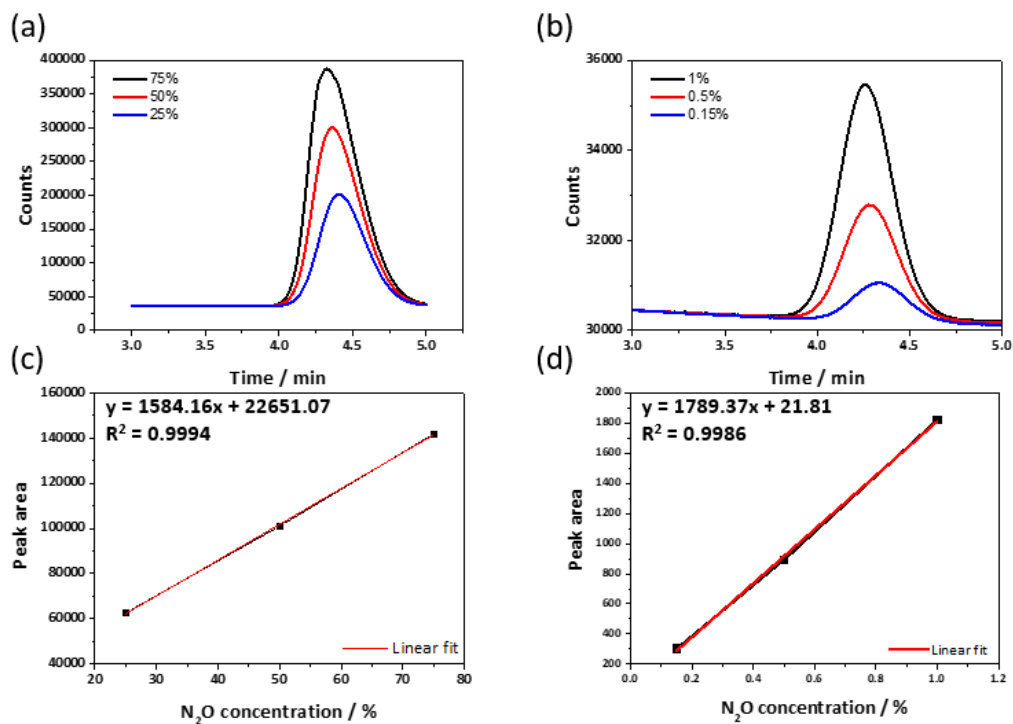
Figure 3.5. N_2O standard gas peak analyzed from GC in (a) high concentration range and (b) low concentration range. Calibration curves between N_2O concentration and peak area of N_2O for (c) high concentration range and (d) low concentration range.
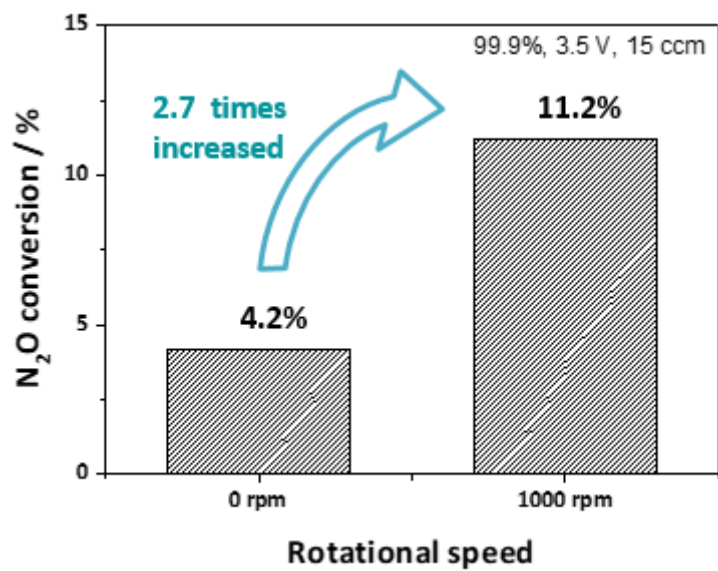
Figure 3.6. N_2O conversion at 0 rpm and 1000 rpm condition.
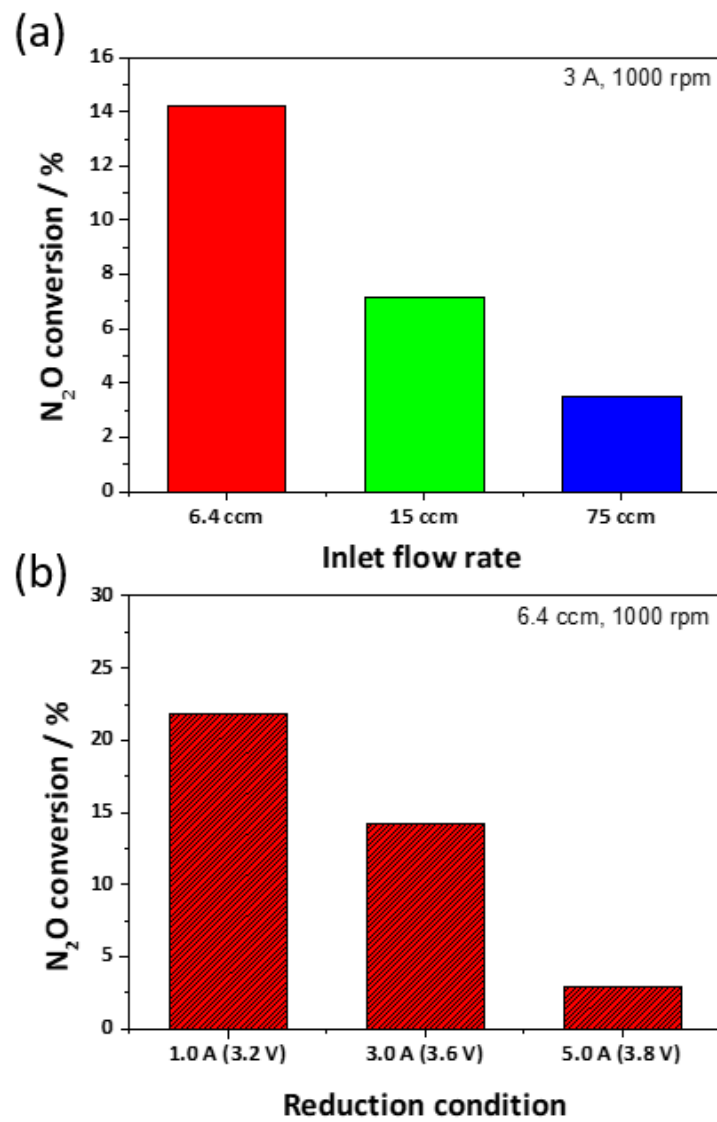
Figure 3.7. N_2O conversion with various reduction conditions. (a) inlet flow rate 6.4, 15, 75 ccm (b) applied current 1.0, 3.0, 5.0 A.

Table 3.2. N_2O Conversion with Various Reduction Conditions.

Working electrode	Inlet N_2O concentration	Applied current / potential	Inlet flow rate	N_2O conversion
Cu foil	99.9%	1.0 A	6.4 ccm	21.9%
		3.0 A	6.4 ccm	14.2%
		5.0 A	6.4 ccm	2.9%
		3.0 A	15 ccm	7.2%
		3.0 A	75 ccm	3.5%
	0.15%	3.0 A	6.4 ccm	13.4%
		3.5 V	6.4 ccm	16.1%
Pd whisker	0.15%	3.0 A	6.4 ccm	59.28%
		3.5 V	6.4 ccm	47.8%
		3.5 V	3.3 ccm	96.18%

3.2 Electrochemical reduction of N_2O with ionic liquid

3.2.1. Optimization of [BMIM][BF$_4$] / PC electrolyte

Figure 3.8 shows LSV curves for the electrochemical reduction of N_2O in the 0.3 M

K_2SO_4 aqueous solution and [BMIM][BF$_4$]. The onset potential of N_2O reduction in the

former solution was–0.8 V, while that of HER was –1.2 V, as shown in Fig. 3.8a. The H_2

gas is one of the byproducts in water electrolysis. The potential gap between the two

reactions was only –0.4 V, and the small gap lowered the N_2O reduction efficiency. For

instance, hydrogen evolution occurred simultaneously with N_2O reduction at –1.3 V,

where the maximum N_2O reduction current density was observed. The close potential of

the two reactions inevitably lowers the efficiency of N_2O reduction. Additionally, the

electrochemical reduction of Cu oxides which was continuously formed in the aqueous

solution further reduced the current efficiency [56]. On the other hand, the gap of onset

potential between N_2O reduction and decomposition of ionic liquid was 1.1 V, which

was larger than that in the aqueous solution (Fig. 3.8b). At the peak potential of N_2O

reduction (–1.9 V), no side reaction appeared to occur. This is a great advantage in terms

of the N_2O reduction efficiency. However, the reduction current density of [BMIM][BF$_4$]

was lower than that of aqueous solution due to the low conductivity and high viscosity of pure [BMIM][BF$_4$] [57, 58]. To improve these properties, PC, a dipolar solvent commonly used in electrochemistry, was mixed in [BMIM][BF$_4$]. PC has a relatively low viscosity (2.5 cP) and it is electrochemically inert [59, 60].

Fig. 3.9 shows the viscosity and electrical conductivity of [BMIM][BF$_4$] and PC mixture solutions depending on the [BMIM][BF$_4$] content. The viscosity of [BMIM][BF$_4$] is much higher (110.3 cP) than that of PC, and the viscosity increased as the [BMIM][BF$_4$] content increased. On the other hand, the electrical conductivity of the solution was maximized at 45 vol% [BMIM][BF$_4$] because it was affected by not only viscosity, but also ion concentration [61]. Increasing the [BMIM][BF$_4$] concentration would increase the ion concentration and viscosity. Thus, the ion mobility which is an important factor of the conductivity, might decrease at higher [BMIM][BF$_4$] concentrations. The solubility and stability of N$_2$O in the solution are also critical factors in the electrochemical reduction of N$_2$O. As shown in Fig. 3.10a, the peak current densities measured from the LSV curves (-1.9 V) at various [BMIM][BF$_4$]/PC compositions did not match with the results with Fig. 3.9. The highest reduction current density was observed at 75 vol% [BMIM][BF$_4$]. The reason seemed that the N$_2$O solubility and stability depend on the [BMIM][BF$_4$] content. A polar gas like N$_2$O

dissolves in the space between the cations and the anions of ionic liquids [62-64]. Therefore, the solubility and stability of N_2O in [BMIM][BF_4]/PC solutions generally decreases as the [BMIM][BF_4] concentration decreases. Fig. 3.10b shows the change in the peak current density (measured at -1.9 V) with the CV cycles (from -0.2 V to -2.0 V) in the [BMIM][BF_4]/PC solution after N_2O saturation for 1 h. The lower the concentration of [BMIM][BF_4] was, the faster was the peak current density decrease with the CV cycles. This indicates that the solubility and stability of N_2O decreases with decreasing [BMIM][BF_4] concentration. Fig. 3.10c shows the ratio of the peak current density of the fourth cycle (i_{4th}) to the peak current density of the first cycle (i_{1st}). Only 35.6% of i_{1st} remained at 45 vol% [BMIM][BF_4], while 96.1% was retained at 100 vol% [BMIM][BF_4]. At 75 vol% [BMIM][BF_4], the current ratio was 88.9%. Therefore, the optimal composition was determined as 75 vol% [BMIM][BF_4] ([BMIM][BF_4]:PC = 75:25) for electrochemical N_2O reduction, considering the electrical conductivity in the solution and the solubility and stability of N_2O.

3.2.2. Current efficiency and Faradaic efficiency of N_2O reduction

Electrochemical reduction of N_2O was conducted with chronoamperometry in 0.3 M K_2SO_4 aqueous solution and the 75 vol% [BMIM][BF$_4$]/PC solution, as shown in Fig. 3.11. In both solutions, the reduction current density decreased remarkably in the early stages and reached a steady state later. In the aqueous solution (Fig. 3.11a), 2.7 mA cm^{-2} measured at 1800 s was observed without dissolved N_2O. This current density seemed mainly attributed to the HER and the reduction of Cu oxides on the surface of working electrode. On the contrast, almost zero current density was observed in the 75% [BMIM][BF$_4$]/PC solution without dissolved N_2O (Fig. 3.11b). The small reduction current density obtained at the early stages seemed to be associated with the instantaneous reduction of pre-formed Cu oxides. In both solutions, during continuous N_2O supply (with dissolved N_2O), higher reduction current density was observed compared to that during Ar purging owing to the electrochemical reduction of N_2O. Fig. 3.11c shows the current efficiency for the electrochemical reduction of N_2O. In the aqueous solution, the current efficiency of N_2O reduction decreased from 83.9% to 49.6% until 1800 s because the proportion of the HER reaction increased over time. However, the current efficiency in the 75 vol% [BMIM][BF$_4$]/PC solution was maintained at over

95% during the measurement. This indicates that few side reactions occurred. The reason of the slight increase in the efficiency observed in the early stages might be the Cu oxide reduction. After 1 h, the faradaic efficiency was measured with the amount of outlet N_2 gas which is the product of N_2O reduction (Fig. 3.11d). A high faradaic efficiency of 90.2% was shown in the 75 vol% [BMIM][BF$_4$]/PC solution. On the contrary, the faradaic efficiency obtained in the aqueous solution was only 41%.

Additionally, considering the environmental aspect, it is possible to compare the electrical energy used for the decomposition of N_2O and the CO_2 emitted to produce the electrical energy. The GWP of N_2O is 310, and it is possible to compare how much environmental value the decomposition efficiency of N_2O has compared to CO_2 emission through the following equation.

$$\frac{N_2O}{CO_2} = \frac{310}{18.64 \frac{mol}{kWh}} \times Faradaic\ efficiency \times current\left(\frac{C}{s}\right) \times \frac{3600s}{1h} \times \frac{1000}{nFVA}$$

Based on our result, the value of N_2O reduction is 123 times in [BMIM][BF$_4$]/PC solution and 106 times in aqueous solution.
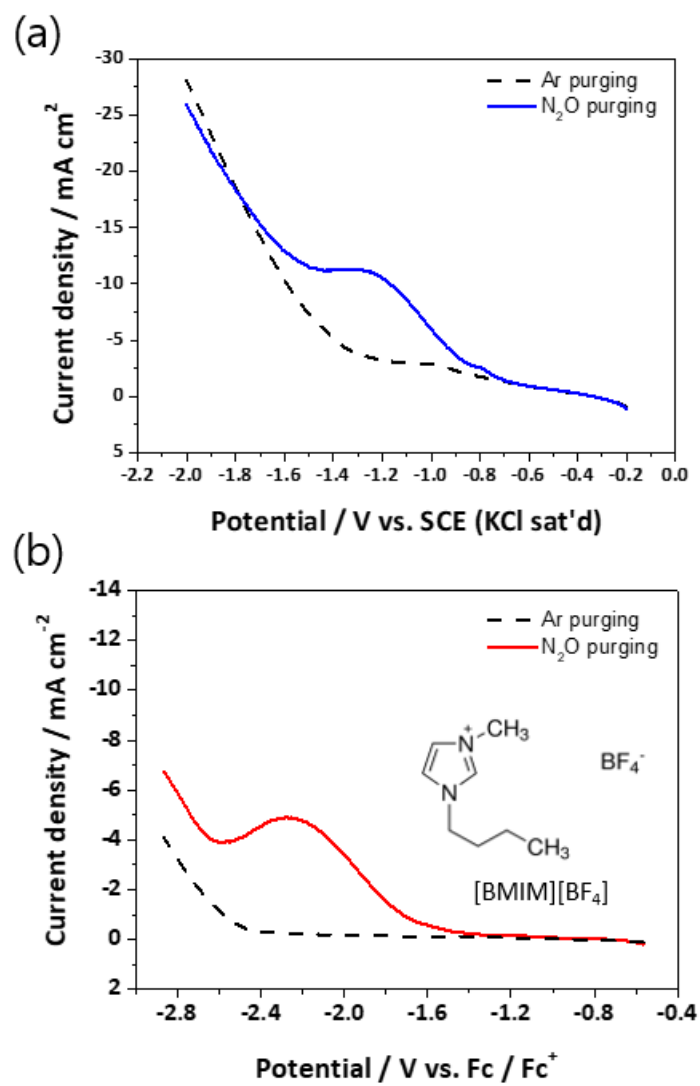
Figure 3.8. LSV curves for Cu electrode in (a) 0.3 M K_2SO_4 aqueous solution and (b) [BMIM][BF$_4$]. The scan rate was 50 mV s^{-1}.
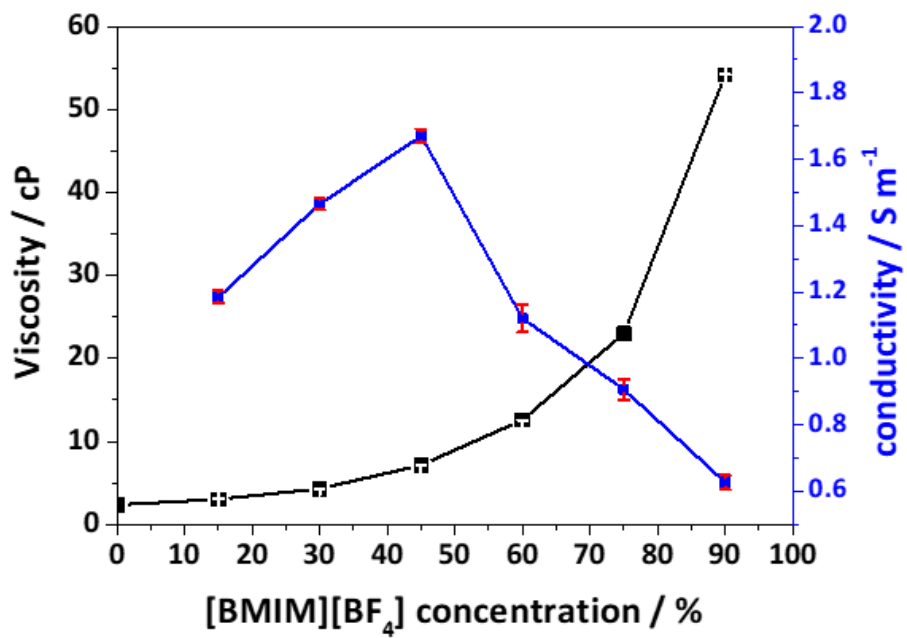
Figure 3.9. Viscosity (black line) and conductivity (blue line) changes for [BMIM][BF$_4$]/PC according to [BMIM][BF$_4$] content.
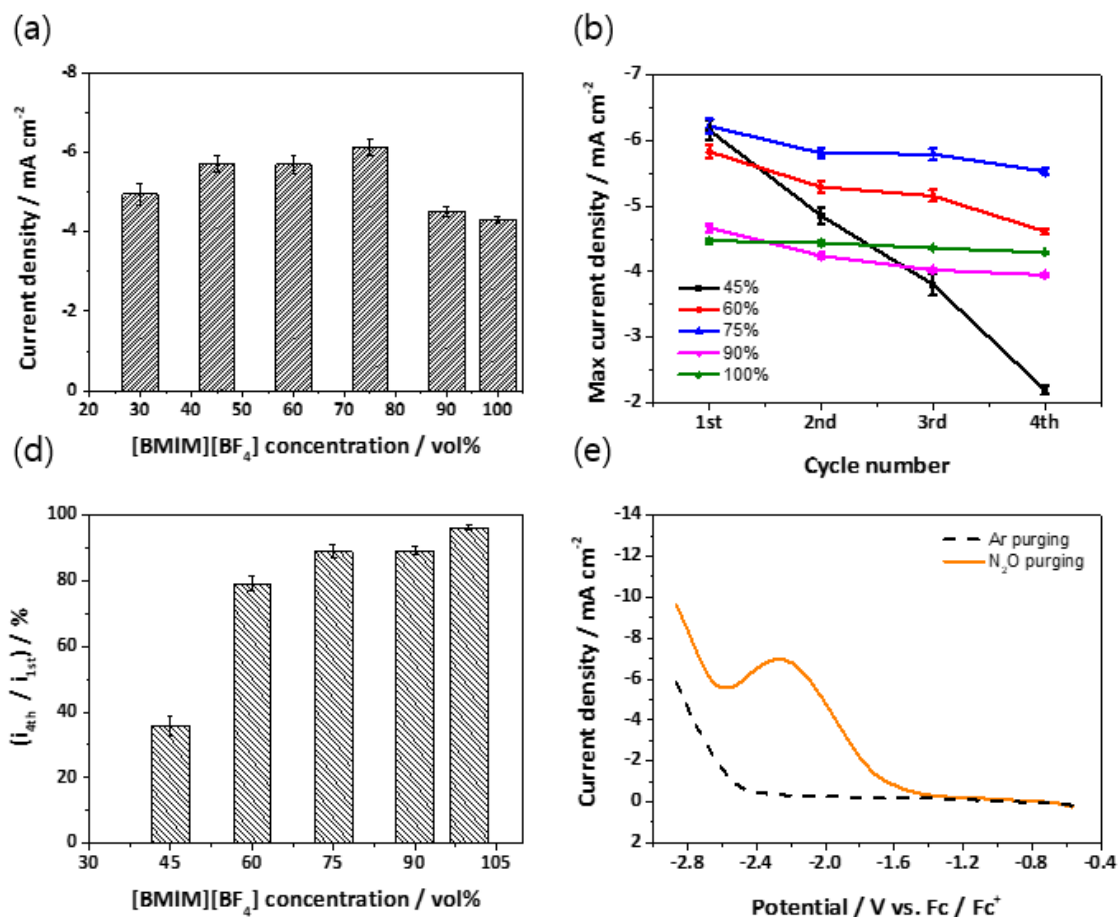
Figure 3.10. (a) reduction current densities measured at -2.27 V (vs. Fc/Fc$^+$), (b) reduction current density at -2.27 V (vs. Fc/Fc$^+$) for different numbers of CV cycles ([BMIM][BF$_4$] concentrations of 45%, 60%, 75%, 90%, and 100%), (c) ratio of the reduction current density at -2.27 V vs. Fc/Fc$^+$ in the fourth cycle (i$_{4th}$) to that in the first cycle (i$_{1st}$). and (d) LSV curve for Cu electrode in the optimized [BMIM][BF$_4$]/PC. The scan rate for both CV and LSV was 50 mV s^{-1}.
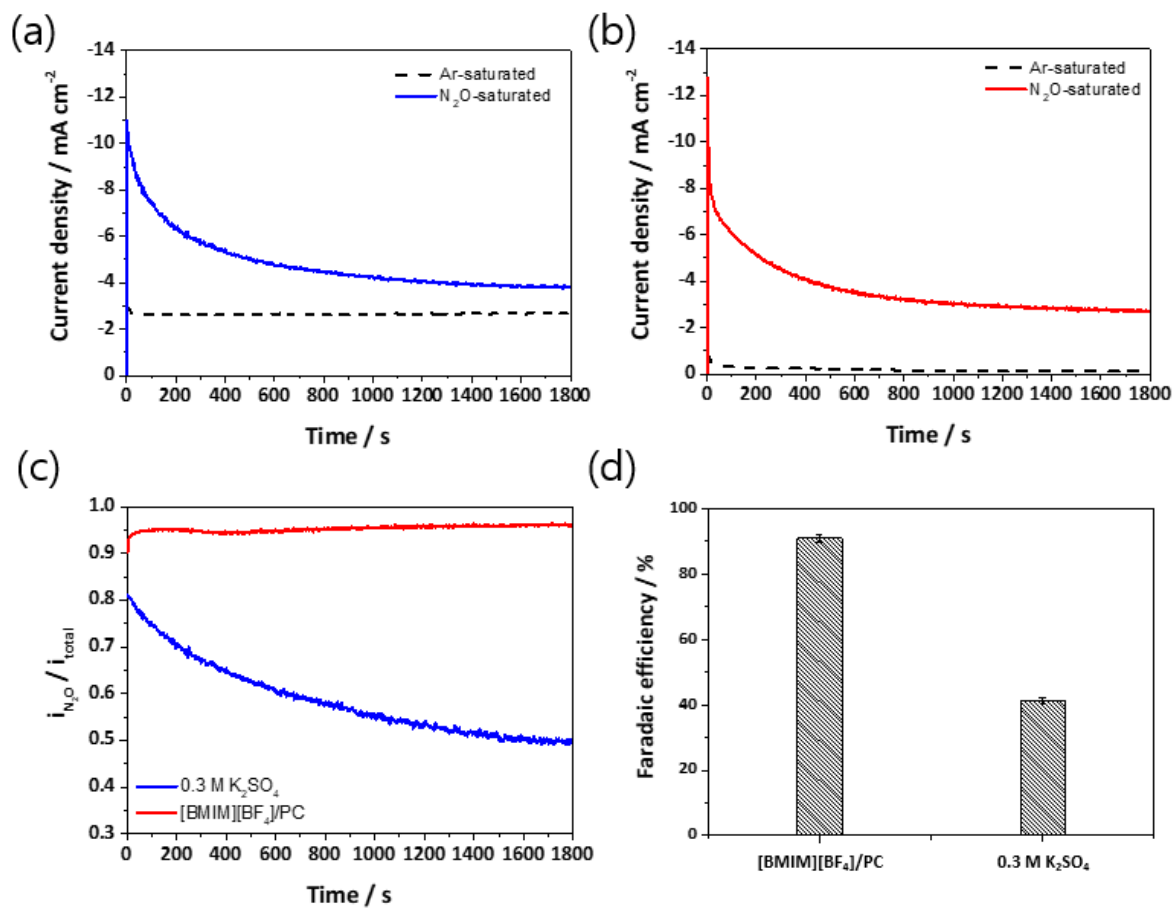
Figure 3.11. Current density-time curves recorded (a) at -1.3 V vs. SCE in 0.3 M K_2SO_4

aqueous solution and (b) at -2.27 V vs. Fc/Fc$^+$ in 75 vol% [BMIM][BF$_4$]). (c) and (d)

show current and Faradaic efficiencies, respectively, in 0.3 M K_2SO_4 aqueous solution

and 75 vol% [BMIM][BF$_4$]).

3.3 Direct electrochemical reduction of SiO_2 in $CaCl_2$ molten salt

3.3.1. Electrochemical analysis of SiO_2 reduction

CV was performed on graphite crucibles containing SiO_2 particles with or without Al (Fig 3.12). Without Al, the electrochemical reduction of SiO_2 particles was observed at negative potentials below -0.4 V. The sharp increase in the reduction current density below -1.0 V was associated with the electrochemical reduction of Ca^{2+} ions, which was also observed at the bare graphite crucible containing no SiO_2 particles. In the reverse scan, two oxidation peaks related to the oxidation of Ca and Si that were reduced in the forward scan were observed at -1.0 and -0.25 V, respectively. This electrochemical behavior of SiO_2 in molten $CaCl_2$ corresponds well with the previous reports [29, 41, 42]. When Al was introduced, the SiO_2 reduction started at a more positive potential (at about -0.1 V) than -0.4 V, indicating that the reduction reaction was promoted by Al. It is assumed that this is due to the two effects of Al. One is that Al, which has a low melting point (660.3°C) [50], becomes a liquid state and enlarges electrical contact area for SiO_2 reduction. The large contact area between the solid SiO_2 and the working electrode (graphite crucible in this case) may facilitate the electrochemical reduction of SiO_2 [65, 66].

The other is the formation of Al-Si alloys. In the course of the SiO_2 reduction, the reduced Si reacts with Al to form Al-Si alloys because the formation of Al-Si alloys is thermodynamically favorable at higher temperature above 577 °C [67]. The formed Al-Si alloys are liquid in 850°C molten $CaCl_2$ until the Si composition reaches 32 at% [67]. This may also accelerate the reduction process of SiO_2. Furthermore, the liquid Al-Si alloys may act as a catalyst for SiO_2 reduction, similar to Ag-Si eutectic droplets [43].

The electrochemical reduction of SiO_2 was then performed, based on the obtained CV curves in Fig. 3.13, by applying a constant reduction current in the potential range where SiO_2 reduction occurs. Fig. 3.13a shows the potential-time curves obtained during the SiO_2 reduction at various reduction currents. The reduction potential decreased with increasing the reduction current, and 60 mA was selected as the reduction current for further experiments because the potential was stably maintained in the potential region (-0.6 – -1.2 V) where the SiO_2 reduction proceeds. It is noteworthy that the potential of SiO_2 reduction with Al at 60 mA was more positive than that without Al. This is in good agreement with Fig. 3.12. The addition of Al also significantly affected the morphology of Si reduced at 60 mA. The Si morphologies after the SiO_2 reduction without and with Al are shown in Figs. 3.13b and c. In the absence of Al, the reduced Si appeared in the form of agglomerated particles similar to those frequently observed in the reduction of

60

SiO$_2$ particles in molten CaCl$_2$ [32, 35]. However, in the presence of Al, the reduced Si showed a single and continuous Si film. It is assumed that this difference is attributed to the formation of liquid Al-Si alloys. According to previous reports on the electrochemical reduction of SiO$_2$ with Ag, the small Ag-Si eutectic droplets formed during the reduction process individually serve as reduction points where Si nucleates and grows in the form of nanorods or dendrites [43]. Al-Si also appears to play a similar role to Ag-Si, but Al-Si is presumed to provide more continuous and larger reduction sites for Si to nucleate and grow during SiO$_2$ reduction than Ag-Si because of low melting temperature of Al-Si. The composition range in which liquid Ag-Si that effectively induces Si nucleation and growth at a molten salt temperature of 850°C can exist is very limited, about 10–12 at$_{Si}$% [68]. Therefore, during the electrochemical reduction of SiO$_2$, Ag-Si in the liquid state can exist only in a small amount, and eventually appears in the form of small droplets. These droplets serve as individual nucleation sites, resulting in the growth of Si nanorods or dendrites. On the other hand, at the same temperature, Al-Si is in a liquid state in a wider composition range (0–32 at$_{Si}$%) than Ag-Si [50, 69]. Therefore, it is presumed that the abundant liquid-state Al-Si induces Si nucleation and growth in a larger area than the Ag-Si, forming a single and continuous Si film.

3.3.2. Properties of reduced Si with Al

In order to investigate the effect of Al on electrochemical reduction of SiO_2, cross sectional optical images of graphite crucible were observed after the reduction for 0, 1,000, and 3,000 s, as shown in Fig. 3.14. Fig. 3.14a shows the graphite crucible containing SiO_2 particles before electrochemical reduction. After applying current of 60 mA for 1,000 s, a 0.27 (±0.07)-mm-thick black film was formed at the bottom and sidewalls of the crucible (Fig. 3.14b). This film became thicker up to 0.54 (±0.03) μm as the reduction time increased to 3,000 s (Fig. 3.14c). Fig. 3.15a shows the XRD patterns of the products inside graphite crucibles after $CaCl_2$ removal, as a function of reduction time. As the reduction time increases, the intensity of the peaks associated with crystalline Si increases while that of SiO_2 peaks decreases. This indicates that SiO_2 was reduced to Si. Fig. 3.15b shows the SEM image and EDS elemental analysis results of the black film. The film was continuous, and its composition was mostly composed of Si (93.16 at%). This indicates that the SiO_2 particles were electrochemically reduced to a continuous Si film in the presence of Al. The growth of the Si film starts at the bottom and sidewalls of the crucible, the initial three-phase boundaries where the conductor (graphite crucible), SiO_2, and molten $CaCl_2$ meet together. On the upper part of the Si

film, a light gray region in which a large amount of Si and O was detected along with a small amount of Al was observed, as shown in Figs. 3.14b, c, and 3.15c. This region is presumed to consist of unreduced SiO_2 particles, and Al and Al-Si alloys[70, 71]. In particular, Al was evenly distributed throughout this region (Fig. 4f), indicating that the liquid Al and Al-Si alloys at 850 °C were uniformly mixed with the SiO_2 particles. Based on Fig. 3.14, we can propose an approximate mechanism of SiO_2 electrochemical reduction in the presence of Al. Al forms liquid Al-Si alloys in 850 °C $CaCl_2$ with electrochemically reduced Si on the surface of electrode. The continuous SiO_2 reduction accumulates Si in the Al-Si alloys, and the Si concentration in Al-Si alloys eventually exceeds the limit (32 at_{Si}%) that the Al-Sl alloy can form. This leads to supersaturation of Si in the alloy and precipitation of solid Si. This concept of mechanism was also introduced in SiO_2 electrochemical reduction with Ag and Ge electrodeposition [43, 72]. In these reports, the products Si and Ge were formed in the form of dendrites. However, in this study, a continuous Si film was obtained. The cause of this phenomenon is not clear, but as mentioned above, it may be because the large amount of Al-Si present in the liquid phase at 850 °C provides a sufficient number of nucleation sites to form a Si film.

3.3.3. On off time optimization and Si film

Figure 3.16a shows the potential-time curve of a graphite crucible containing Al and

SiO$_2$ particles at an applied reduction current of 60 mA. Without off time, the electrode

potential continuously decreased during the reduction. In particular, after 2,000 s, the

electrode potential rapidly decreased to below -1.2 V, a potential region where the

electrochemical reduction of Ca^{2+} ion occurs predominantly. This negative potential shift

lowers the electrochemical reduction efficiency of SiO$_2$. This is a common phenomenon

in the electrochemical reduction of SiO$_2$, and the main cause of this phenomenon is that

oxygen ions released during the reduction process of SiO$_2$ accumulate at the three-phase

boundaries and interfere with the SiO$_2$ reduction [73]. A pulsed current was introduced to

alleviate this phenomenon. Pulsed currents of various on/off time conditions were

applied for SiO$_2$ reduction, and Fig. 3.16a shows the potential-time curve for an on/off

time of 250/125 s. With the introduction of off time, the electrode potential was

maintained within the potential range (-0.6 – 1.2 V) where SiO$_2$ reduction predominantly

occurs for a 46.81% longer period of time (on time basis) than when off time was not

introduced. The introduction of off time offers two advantages for the stable

electrochemical reduction of SiO$_2$. The one is that off time provides liquid Al and Al-Si

alloys with time to rearrange to establish new three-phase boundaries between the conductors (Si and liquid Al-Si alloys), SiO_2, and molten $CaCl_2$ after SiO_2 was electrochemically reduced during the on time. The other is that the oxygen ions produced during the reduction of SiO_2 diffuse out during the off time. With various on/off time conditions, the effective charge (the charge consumed in the potential range more positive than -1.2 V) and the thickness of Si films were measured, as shown in Figs. 3.16b. The effective charge and the Si film thickness are proportional to each other, indicating that the effective charge is actually consumed for the SiO_2 reduction. The effective charge and thickness of Si film were 205.53 C and 0.76 mm at 250/125 condition.   Longer on time decreased the effective charge because the higher ratio of on time brings the lower effect of off time. Especially, the 1000/125 condition had little difference with w/o off time condition (5% increase in effective charge). On the other hand, the effective charge increased to 232.36 C when the on time was reduced to 125 s, and there was no significant change below the on time of 125 s. 125 s of off time seemed to be sufficient time to let molten $CaCl_2$, liquid Al, and Al-Si alloys to form three-phase and to let the dissolved O^{2-} ions diffuse away for on time below 125 s. Among the tested conditions, the highest effective charge (232 C) was achieved at 125/125 s of on/off time.

Fig. 3.17 and 3.18 show the characteristics of a Si deposit at the optimized condition. Right after the electrochemical reduction and before the washing process, of the bulk Si deposit was obtained as shown in Fig. 3.17a. The thickness of the Si film was 0.86 ($\pm$ 0.21) mm, which was 59% increased value compared with that of the Si film without off time (0.54 mm). Highly-magnified SEM images of Si film surface (Fig. 3.17b) show that the surface of Si film has flat and planar morphology. The EDS spectrum of the Si film suggested that the Si ratio was quite pure (>96%) and some other materials were oxygen and Al. Ca, and Cl was under the detection limit (Fig. 3.18). Small amount of oxygen was detected because of little unreacted SiO_2 and native oxide formed on the Si film. Since Al-Si forms an alloy in a wide range, high purity of Si may not be expected. However, this high purity of Si film supports the segregation mechanism during electrochemical reduction of SiO_2. With the further development of this study, it is expected to substitute the existing Si fabrication processes with direct electrochemical reduction method.
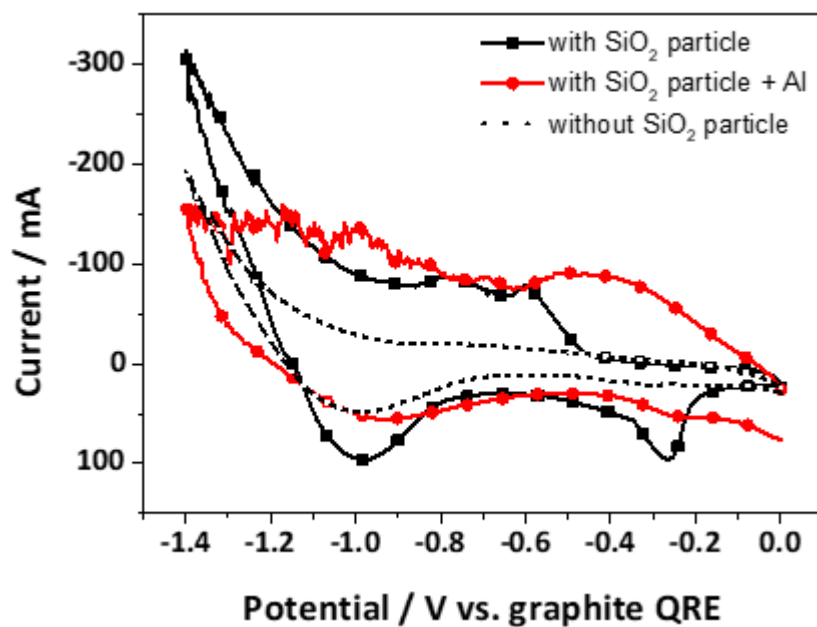
Figure 3.12. Cyclic voltammograms for graphite crucible electrode in molten $CaCl_2$ (850 °C) at a scan rate of 50 mVs^{-1} with SiO_2 particle, without SiO_2 particle, and with Al eutectic catalyst.
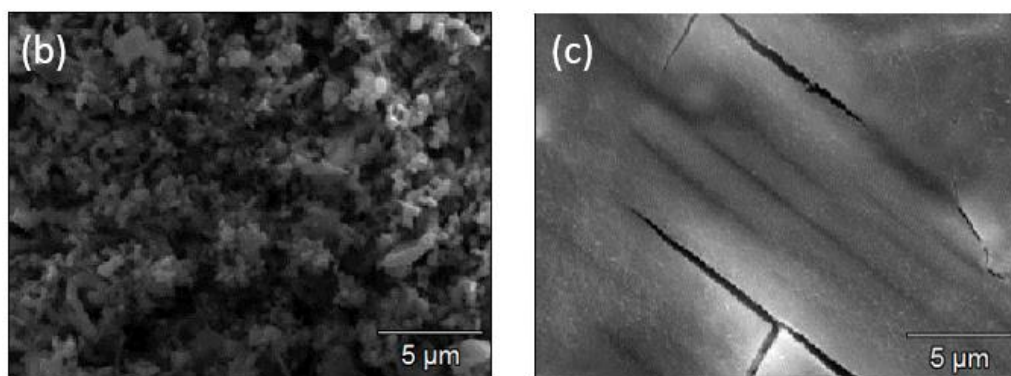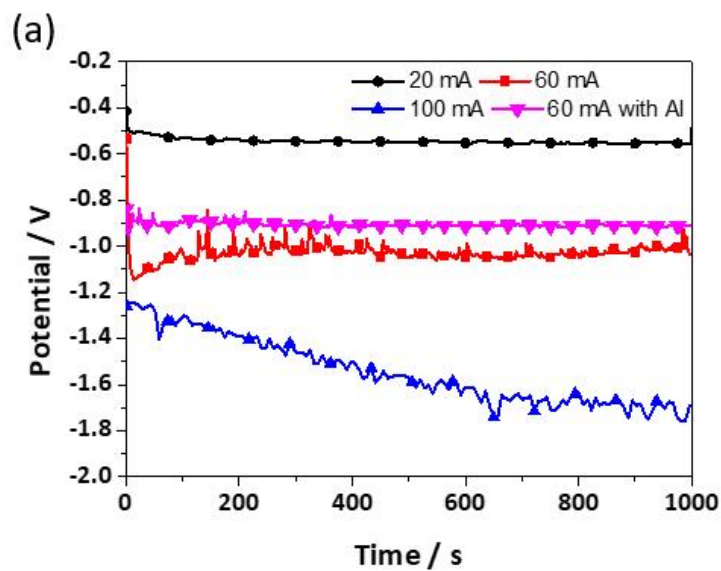
Figure 3.13. (a) Chronopotentiometry for graphite crucible electrode containing SiO$_2$ particles at 20, 60, 100 mA in molten CaCl$_2$ (850 $^\circ$C). SEM images of the silicon deposited at 60 mA for 3000 s on graphite crucible electrode (b) without Al eutectic catalyst and (c) without Al eutectic catalyst.
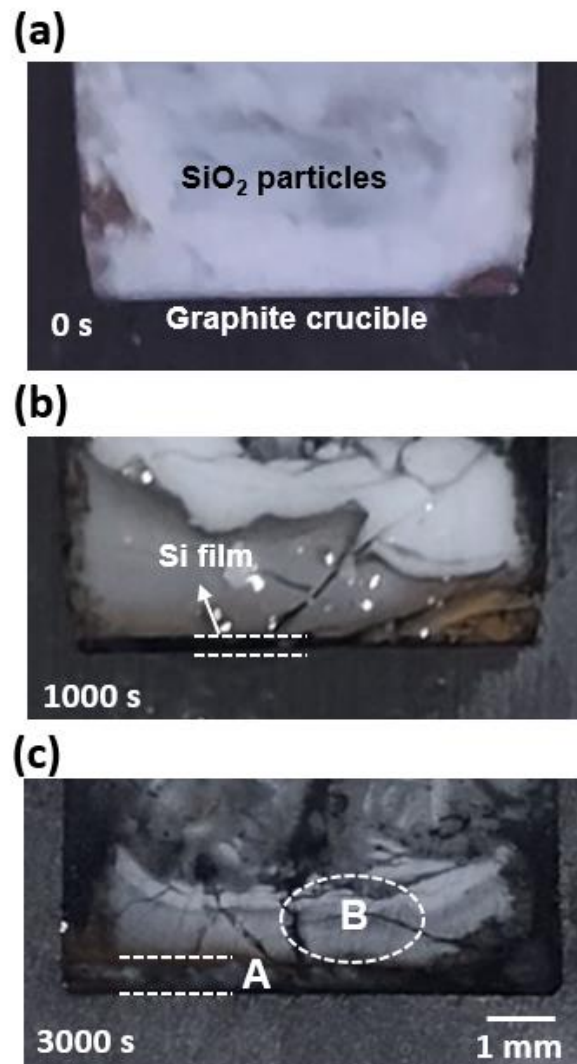
Figure 3.14. Cross sectional optical images of silicon deposit and silicon dioxide in graphite crucible at 60 mA for (a) 0, (b) 1000, and (c) 3000 s, respectively.
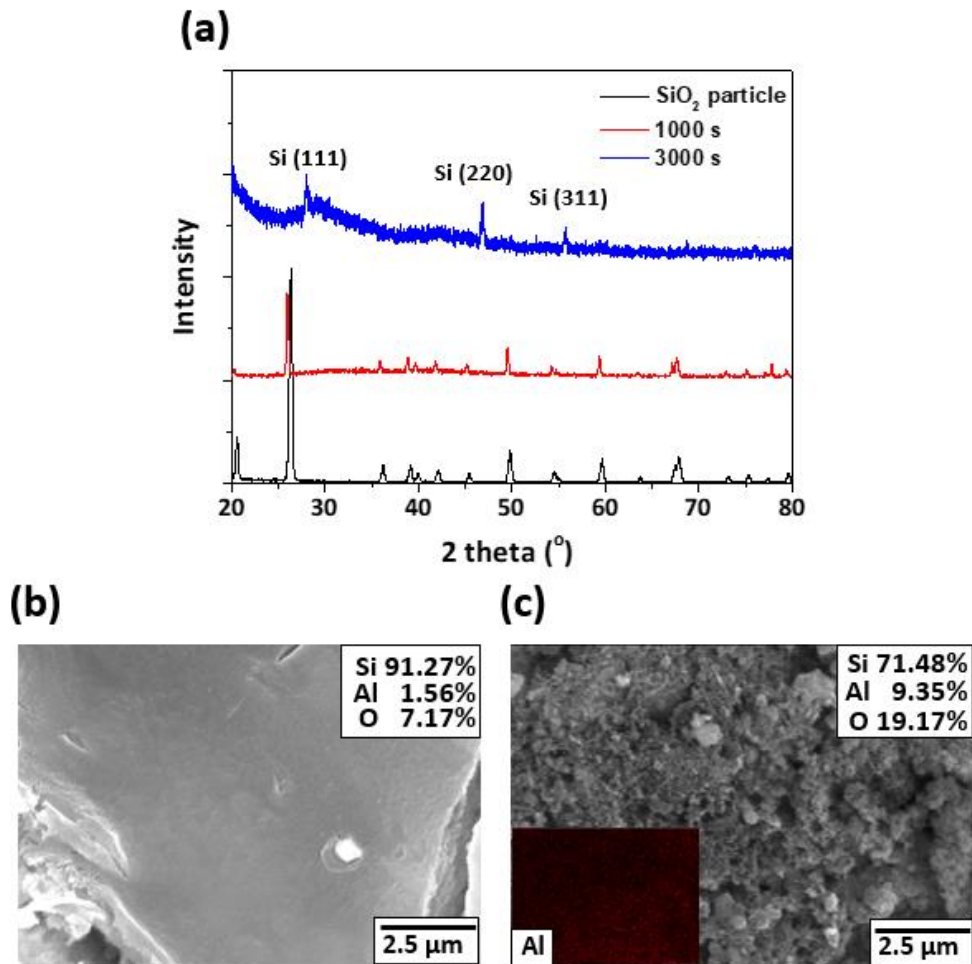
Figure 3.15. (a) X-ray diffraction spectrums of the deposits. SEM image and atomic

ratio measured with EDS mapping of (b) black deposit and (c) gray deposit (at 60 mA

for 3000 s). EDS mapping of Al was shown in red dots.
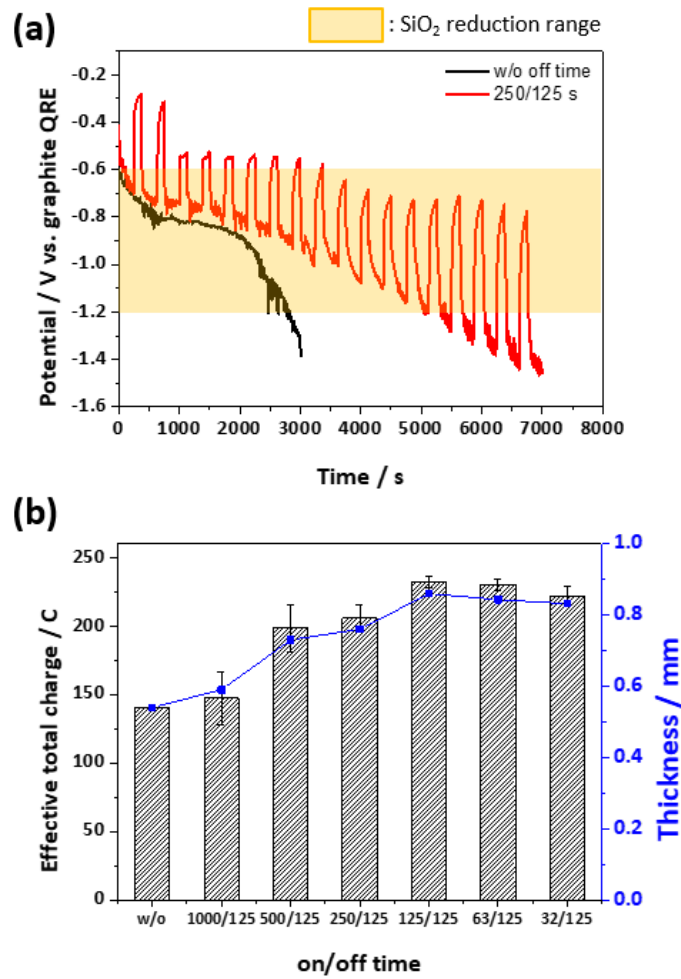
Figure 3.16. Optimization of on/off time control. (a) Chronopotentiometry for graphite

crucible at 60 mA without off time and 250/125 s. (b) Effective total charges of

chronopotentiometry and Si film thickness at each on/off time conditions (1000/125,

500/125, 250/125, 125/125, 63/125, 32/125).
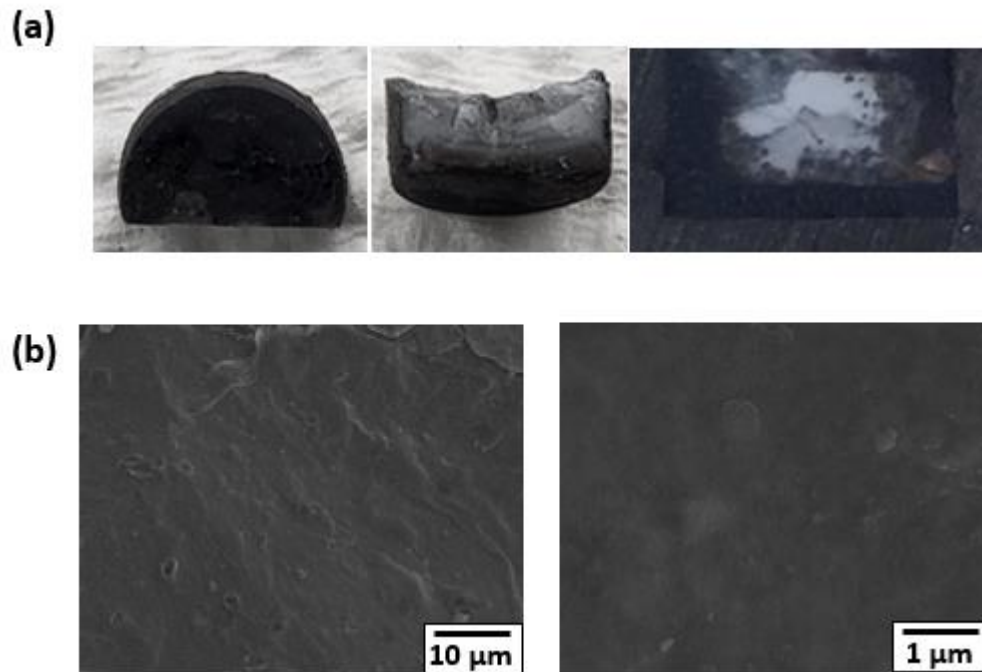
Figure 3.17. Properties of Si film with optimized condition (reduced at 60 mA for 125/125 on/off time with 40 repetitions). (a) optical images of Si film (b) SEM images of Si film (c) EDS spectrum and atomic ratio of Si film.
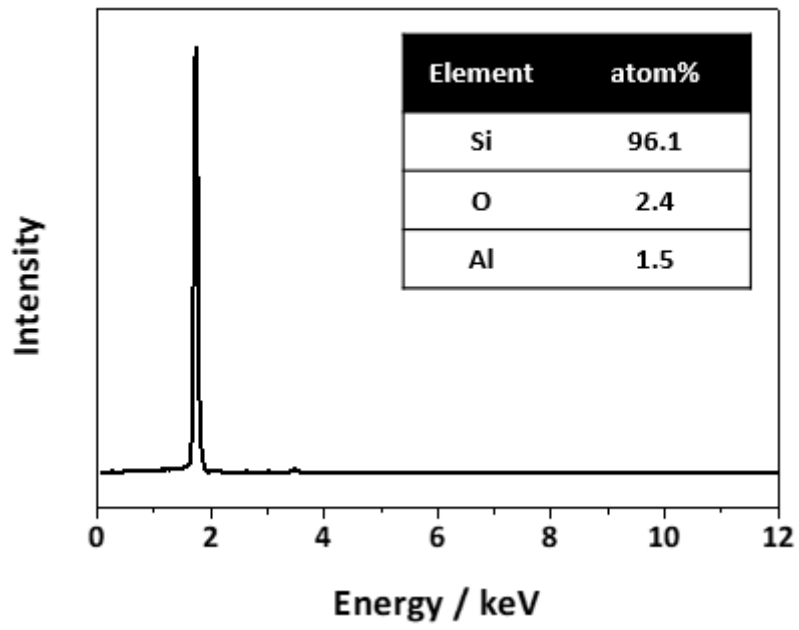
Figure 3.18. EDS spectrum and atomic ratio of Si film.

CHAPTER IV

Conclusion

Couette-Taylor vortex reactor was adopted to electrochemical reduction of N_2O. in the CTVR, the N_2O dissolution in aqueous solution was dramatically improved. At 1000 rpm, the dissolution time need for saturation was decreased from 30 min to 2 min compared with 0 rpm condition. The solubility of N_2O was also increased from 24.3 mM to 30.5 mM with Taylor vortex. Increased volumetric diffusion coefficient and bubble pressure influenced by Taylor vortex were effective for N_2O dissolution. The conversion of N_2O was also increased from 4.2% to 11.2% during electrochemical reduction at 1000 rpm Taylor condition. Considering the degree of increase in conversion, the dissolution rate was critical at continuous flow reduction system. The electrochemical reduction system parameters were also investigated in the terms of N_2O conversion. The faster the flow rate of N_2O, the lower N_2O conversion was obtained as throughput increased. In addition, excessive applied current leads to a decrease in N_2O conversion because it causes high electrical potential and resulting dominant HER generation.

[BMIM][BF_4]/PC solutions were used as an electrolyte instead of an aqueous solution for the electrochemical reduction of N_2O. In order to enhance N_2O reduction, the

composition of the [BMIM][BF$_4$]/PC solution was optimized with consideration of the electrical conductivity, N$_2$O solubility and stability. At 75 vol% [BMIM][BF$_4$], a higher current density and faradaic efficiency of N$_2$O reduction were observed compared with in a 0.3 M K$_2$SO$_4$ aqueous solution. Elimination of the HER and Cu oxide formation, which are possible side reactions in an aqueous solution, brought the high current density and faradaic efficiency. The higher solubility and stability of N$_2$O observed in [BMIM][BF$_4$] compared with those in aqueous solution also attributed to these improvements. This study has experimentally demonstrated that the efficiency of N$_2$O reduction can be improved using a non-aqueous ionic liquid electrolyte instead of aqueous solution.

SiO$_2$ particles was transformed by electrochemical reduction to pure Si film in 850 °C molten CaCl$_2$. SiO$_2$ particles were contained in graphite crucible working electrode and changed to liquid Al-Si alloy during electrochemical reduction. Potential shift and effective potential range of SiO$_2$ reduction was confirmed by cyclic voltammetry in the presence of Al. Si film deposited with Al had flat surface which was caused from the formation of liquid phase of Al-Si alloy. The reaction process and formation of Al-Si alloys in the crucible during electrochemical reduction was observed with optical image, SEM, EDS, and XRD analysis. Furthermore, electrochemical reduction process was

optimized with applying on/off time and charge amount for SiO_2 reduction could be increased. The off time seemed to offer enough time to form three-phase interface between Al-Si alloys and molten $CaCl_2$, and to diffuse away O^{2-} ions. Si film deposited with optimized condition was analyzed with optical image, SEM, and EDS. The thickness of Si film was 59% increased with optimized on/off time condition. The flat Si film was fabricated and the Si content was quite pure (>96%). It is expected that direct electrochemical reduction of SiO_2 with Al would replace the existing inefficient Si fabrication processes with further study.

References

1.   Nakaso, K., et al., *Chem. Eng. Sci.* **58**: p. 3327-3335. (2003).

2.   Liberman, M.A., A.D. Kiverin, and M.F. Ivanov, *Phys. Lett. A*. **375**: p. 1803-1808. (2011).

3.   Zagal, J.H., *Coord. Chem. Rev.* **119**: p. 89-136. (1992).

4.   Savéant, J.-M., *Chemical Reviews*. **108**: p. 2348-2378. (2008).

5.   Marcus, R.A., *Annu. rev. phys. chem.* **15**: p. 155-196. (1964).

6.   He, Z.D., et al., *Angew. Chem. Int. Ed.* **57**: p. 7948-7956. (2018).

7.   Kroeze, C., *Sci. Total Environ.* **143**: p. 193-209. (1994).

8.   Ravishankara, A.R., J.S. Daniel, and R.W. Portmann, *Science*. **326**: p. 123-125. (2009).

9.   Crutzen, P.J., *Quarterly Journal of the Royal Meteorological Society*. **96**: p. 320-325. (1970).

10.   Shankman, S. *Global N2O emission trend*. 2019   [cited 2022 5.17.]; Available from: https://insideclimatenews.org/news/11092019/nitrous-oxide-climate-pollutant-explainer-greenhouse-gas-agriculture-livestock/.

11.   N Van den Heuvel, R., et al., *Geobiology*. **9**: p. 294-300. (2011).

12.   Konsolakis, M., *ACS Catalysis*. **5**: p. 6397-6421. (2015).

13.   Liu, Z., et al., *Catalysis Surveys from Asia*. **20**: p. 121-132. (2016).

14.   White, F., *New York, USA*. 52-78. (2003).

15.   Youd, A.J. and C.F. Barenghi, *Phys. Rev. E*. **72**: p. 056321. (2005).

16.   Baek, S., et al., *Applied Catalysis B: Environmental*. **217**: p. 313-321. (2017).

17.   Baek, S., et al., *Chemical Engineering Journal*. **335**: p. 915-920. (2018).

18.   Kudo, A. and A. Mine, *Journal of Electroanalytical Chemistry*. **426**: p. 1-3.
(1997).

19.   Kim, K.H., et al., *Electrochem. Commun.* **62**: p. 13-16. (2016).

20.   Villar-Garcia, I.J., et al., *Chem. Sci.* **5**: p. 4404-4418. (2014).

21.   Epstein, E., *Annu. Rev. Plant Physiol.* **50**: p. 641-664. (1999).

22.   Xu, Y., et al., *Sens.* **19**: p. 2908. (2019).

23.   Nordberg, R., et al., *Inorg. Chem.* **9**: p. 2469-2474. (1970).

24.   Braga, A.F.B., et al., *Sol. Energy Mater. Sol. Cells*. **92**: p. 418-424. (2008).

25.   Johnston, M.D., et al., *JOM*. **64**: p. 935-945. (2012).

26.   Safarian, J., G. Tranell, and M. Tangstad, *Energy Procedia*. **20**: p. 88-97. (2012).

27.   Yang, X., et al., *Angew. Chem.* **129**: p. 15274-15278. (2017).

28.   Haarberg, J.X.a.G.M., *High Temp. Mater. Proc.* **32**: p. 97-105. (2013).

29.   Zou, X., et al., *Nat. Commun.* **10**: p. 5772. (2019).

30.   Gopalakrishna M. Rao, D.E., and Robert S. Feigeison, *J. Electrochem. Soc.* **127**: p. 1941. (1980).

31.   Munisamy, T. and A.J. Bard, *Electrochim. Acta*. **55**: p. 3797-3803. (2010).

32.   Nohira, T., K. Yasuda, and Y. Ito, *Nat. Mater.* **2**: p. 397-401. (2003).

33.   Cohen, U., *J. Electron. Mater.* **6**: p. 607-643. (1977).

34.   Elwell, D., *J. Cryst. Growth*. **52**: p. 741-752. (1981).

35.   Cai, J., et al., *J. Electrochem. Soc.* **159**: p. D155-D158. (2012).

36.   Kongstein, O.E., et al., *ECS Trans.* **3**: p. 357-361. (2019).

37.   Huseynov, E., A. Garibov, and R. Mehdiyeva, *J. Electrostat.* **74**: p. 73-78. (2015).

38.   Srivastava, J.K., M. Prasad, and J.B. Wagner, *J. Electrochem. Soc.* **132**: p. 955-963. (1985).

39.   Lee, S.-C., J.-M. Hur, and C.-S. Seo, *Ind. Eng. Chem.* **14**: p. 651-654. (2008).

40.   Ma, Y., et al., *ECS Trans.* **98**: p. 215-222. (2020).

41.   Cho, S.K., F.-R.F. Fan, and A.J. Bard, *Electrochim. Acta*. **65**: p. 57-63. (2012).

42.   Xiao Yang, L.K., Xingli Zou, Taeho Lim, Ji Zhao, Edward T. Yu, and Allen J. Bard, *Angew. Chem. Int. Ed.* **56**: p. 15078-15082. (2017).

43. Sung Ki Cho, F.-R.F.F., and Allen J. Bard, *Angew. Chem.* **124**: p. 12912-12916. (2012).

44. Carretero-Genevrier, A. and N. Mestres, *Growth of 1-D Oxide Nanostructures*, in *Encyclopedia of Nanotechnology*. 2015.

45. Peng, J., et al., *Adv. Func. Mater.* **28**: p. 1703551. (2018).

46. Revelli, A.-L., F. Mutelet, and J.-N. Jaubert, *The Journal of Physical Chemistry B*. **114**: p. 8199-8206. (2010).

47. Weiss, R.F. and B.A. Price, *Marine Chemistry*. **8**: p. 347-359. (1980).

48. Kobatake, H., et al., *J. Mater. Sci.* **50**: p. 3351-3360. (2015).

49. Molina, J.M., et al., *Int. J. Adhes. Adhes.* **27**: p. 394-401. (2007).

50. Murray, J.L. and A.J. McAlister, *Bull. Alloy Phase Diagr.* **5**: p. 74. (1984).

51. Nishihara, H., et al., *Nanoscale*. **6**: p. 10574-10583. (2014).

52. Wang, B. and X.-y. Li, *Anal. chem.* **70**: p. 2181-2187. (1998).

53. Dłuska, E., S. Wroński, and T. Ryszczuk, *Exp. therm. fluid sci.* **28**: p. 467-472. (2004).

54. Wroński, S., R. Hubacz, and T. Ryszczuk, *Chem. Eng. J.* **105**: p. 71-79. (2005).

55. Baek, S., et al., *J. Appl. Electrochem.* **50**: p. 395-405. (2020).

56. Beverskog, B. and I. Puigdomenech, *Journal of The Electrochemical Society*.

144: p. 3476-3483. (1997).

57.   Stoppa, A., et al., *Journal of Chemical & Engineering Data*. **55**: p. 1768-1773. (2010).

58.   Zhou, Q., L.-S. Wang, and H.-P. Chen, *Journal of Chemical & Engineering Data*. **51**: p. 905-908. (2006).

59.   Shi, J., et al., *Journal of Power Sources*. **259**: p. 50-53. (2014).

60.   Payne, R. and I.E. Theodorou, *The Journal of Physical Chemistry*. **76**: p. 2892-2900. (1972).

61.   Seki, S., et al., *Journal of The Electrochemical Society*. **165**: p. A542-A546. (2018).

62.   Chen, Y., F. Mutelet, and J.-N. Jaubert, *Fluid Phase Equilibria*. **372**: p. 26-33. (2014).

63.   Versteeg, G.F. and W.P.M. Van Swaaij, *Journal of Chemical & Engineering Data*. **33**: p. 29-34. (1988).

64.   Tsai, T.-C., et al., *Journal of Chemical & Engineering Data*. **45**: p. 341-347. (2000).

65.   Zhu, P. and Y. Zhao, *RSC Adv.* **7**: p. 26392-26400. (2017).

66.   Bentley, C.L., M. Kang, and P.R. Unwin, *J. Am. Chem. Soc.* **141**: p. 2179-2193.

(2019).

67.   Ye, H., *J. Mater. Eng. Perform.* **12**: p. 288-297. (2003).

68.   Olesinski, R.W., A.B. Gokhale, and G.J. Abbaschian, *Bull. Alloy Phase Diagr.*

10: p. 635-640. (1989).

69.   Hassam, S., et al., *Metall. Mater. Trans. A*. **21**: p. 1877-1884. (1990).

70.   Abboud, J. and J. Mazumder, *Sci. Rep.* **10**: p. 12090. (2020).

71.   Dahle, A., et al., *Mater. Sci. Eng. A*. **413**: p. 243-248. (2005).

72.   Carim, A.I., et al., *J. Am. Chem. Soc.* **133**: p. 13292-13295. (2011).

73.   Lenser, C., et al., *Adv. Funct. Mater*. **24**: p. 4466-4472. (2014).

국문 초록

산화물을 환원시키는 효과적인 방법으로 전기화학적 환원 반응이 널리 이용되고 있다. 전기화학적 환원 반응은 상온 근처의 낮은 공정 온도에서 전극, 촉매, 전해질, 인가 조건 등의 여러 공정 변수를 조절하여 반응 속도와 반응 효율을 향상시킬 수 있어 다양한 연구 가능성을 가진 환원 방법이다. 전기화학적 환원 반응은 특히 수소 발생 반응, 산소 환원 반응, 이산화탄소 환원 방법 등의 기체 산화물 환원과 금속 도금, 고체 연료전지 등의 고체 산화물 환원 분야에 널리 활용되고 있다. 본 연구에서는 유체역학적, 전기화학적 여러 방법을 통해 전기화학적 환원 반응의 반응속도와 효율을 향상시키고자 연구를 진행하였다.

본 연구에서 다룬 기체 산화물인 아산화질소는 세계 온난화 지수가 이산화탄소에 비해 310 배에 달하는 강력한 온실 기체이다. 농경 산업과 각종 산업 등에서 주로 배출되는 아산화질소는 대기중 농도가 계속해서 증가하고 있으며, 대기중에서 오랜 시간 잔류하기 때문에 분해와 저감에 대한 연구가 활발히 진행되고 있다.

아산화질소의 효과적인 전기화학적 환원을 위해 크게 두 가지의 접근 방법을 적용하였다. 첫째로, 쿠에트-테일러 유동 반응기를 전기화학적 시스템에 적용하여 유체역학적 방법을 통해 전기화학적 환원의 반응 속도와

아산화질소 환원 전환율을 증대시키고자 하였다. 전기화학적 환원을 실시하기에 앞서, 쿠에트-테일러 유동 반응기 내에서 아산화질소의 수용액으로의 용해 속도와 용해도를 측정해 테일러 유동이 아산화질소의 용해에 어떠한 영향을 미치는지 확인해 보았다. 테일러 유동의 유무에 따라 아산화질소의 용해도와 용해 속도가 확연한 차이를 보여 주었는데, 특히 테일러 유동이 일어날 때에 용해 속도 측면에서 눈에 띄는 효과를 보여주었다. 이후 아산화질소의 전기화학적 환원 반응을 쿠에트-테일러 유동 반응기 내에서 진행하여 증가된 용해 거동이 전기화학적 분해 반응에 미치는 영향을 확인하였다. 아산화질소의 전환율은 테일러 유동이 없을 때에 비해 2.7 배 증가하였다. 테일러 유동에 의한 물질 전달 속도 증가에서 기인한 아산화질소의 빠른 용해 속도가 위와 같은 전환율 증가를 가져온 것으로 평가된다. 이후 아산화질소의 입구 유량에 따른 전환율 변화와 인가 전류에 따른 전환율 변화를 통해 각 전기화학적 공정변수가 전환율에 미치는 영향을 확인할 수 있었다.

아산화질소의 전기화학적 환원을 개선시키기 위한 또다른 접근법으로 전해질에 이온성 액체를 적용시켜 보았다. 본 연구에 사용된 이온성 액체는 1-butyl-3-methylimidazolium tetrafluoroborate, [BMIM][BF$_4$] 이며, 유기 용매인 프로필렌 카보네이트와 혼합하여 전해질로 사용하였다. 이온성 액체는 수용액 내에서의 주요 부반응인 수소발생반응을 배제하기 위해 사용되었으며, 주로 전기화학적 환원 반응의 효율을 증대시키기 위해

전해질로 사용하였다. [BMIM][BF$_4$]은 수용액에 비해 90 배 이상의 높은 아산화질소 용해도를 갖고 있어 아산화질소의 전기화학적 환원에 적합한 이온성 액체로 평가되었다. 이온성 액체의 낮은 전기 전도성과 높은 점도는 전해질로서의 단점으로 작용하는데, 이는 유기용매인 프로필렌 카보네이트와의 비율 최적화를 통해 최소화할 수 있었다. 최적화된 이온성 액체 전해질 내에서의 전류 효율과 페러데이 효율은 각각 95%, 90% 이상으로 나타났고, 이는 부반응인 수소발생반응을 효과적으로 배제하고 전류의 대부분을 아산화질소 환원에 이용할 수 있었기 때문이라고 생각된다.

본 연구에서 다룬 또다른 산화물로는 고체 산화물인 이산화규소이다. 이산화규소는 일반적으로 전기가 통하지 않는 부도체이나, 전극에 직접 닿은 이산화규소에 전자를 흘려 주어 직접적인 전기화학적 환원 반응이 가능하다는 연구 내용이 발표된 바 있다. 또한 물질전달이 빠르고 이산화규소의 전기화학적 환원 반응의 부산물인 산화 이온을 잘 용해시킬 수 있는 850°C 이상의 염화칼슘 용융염을 전해질로 사용하면 이산화규소의 전기화학적 환원 반응이 가능하다. 또한 알루미늄 금속을 이용하여 알루미늄-실리콘 액체 합금 형성을 통해 전기적 접촉을 향상시키고 환원된 실리콘의 형태를 필름 형태로 만들 수 있었다. 이후 금속 도금 분야에서 활용되고 있는 펄스 도금을 응용하여 최적화를 진행하였다. 전류가 가해지지 않는 시간 동안 알루미늄-실리콘 액체 합금이 형성되는 시간과 생성된 산화 이온의 확산 시간을 확보해 줄 수 있었다. 최적화 된 시간에서

이산화규소 환원 시 오랜 환원 시간과 늘어난 환원 전하량, 두꺼워진 필름 두께를 얻을 수 있었으며, 샘플의 SEM 및 EDS 분석 결과 평평한 필름 표면과 96% 이상의 실리콘 성분을 확인할 수 있었다.